Article:

eprints@whiterose.ac.uk
https://eprints.whiterose.ac.uk/

1 **Particle-Scale Observation of Seepage Flow in Granular Soils Using PIV and CFD**

2 N Sanvitale[1], B.D. Zhao[2], E.T. Bowman[1], C. O'Sullivan[3]

3 [1]Department of Civil and Structural Engineering, University of Sheffield, Sheffield, UK

4 [2]School of Civil Engineering, University College Dublin, Dublin, Ireland (formerly Imperial

5 College London)

6 [3]Department of Civil and Environmental Engineering, Imperial College London, London, UK

7

8 **Abstract**

9 Seepage-induced instabilities pose a challenge in many geotechnical applications. Particle-scale

10 mechanisms govern the initiation of instability. However, current understanding is based on a

11 macro-scale perspective that draws on continuum mechanics. Recent developments in imaging and

12 numerical analysis can provide the particle-scale fundamental perspective needed to develop a

13 comprehensive insight. This contribution demonstrates the value of combining particle-scale

14 experimental and numerical studies. The experiments consider transparent soil samples created

15 using refractive image matching and monitored by particle image velocimetry (PIV). Three-

16 dimensional pore topology is extracted from a series of 2D images and imported into

17 computational fluid dynamics (CFD) simulations. Permeability is estimated by three distinct

18 approaches: using flow rate, PIV- and CFD-generated data. The flow fields obtained from PIV and

19 CFD are in good agreement considering both flow rate contour plots and flow rate distributions;

20 this demonstrates the successful reconstruction of three-dimensional pore structure and flow-field

21 analysis. The comparison also reveals that the side boundary effects in CFD simulations are

22 constrained within a limited region. The multi-plane results characterize the variance of flow

23 velocity with the three-dimensional pore topology. Finally, the fluid-particle interactions obtained

24 from CFD results show a larger variance in the angular particle packings.

25

26 **Keywords:** Particle-scale behaviour; permeability; seepage; laboratory tests; numerical modelling

27

28 **Corresponding author:** Budi Zhao (budi.zhao@ucd.ie)

29

30 **1. Introduction**

31   A comprehensive understanding of seepage flow in cohesionless or granular soils is critical in

32 many geotechnical analyses associated with dewatering, dam and flood embankment design, slope

33 stability etc. Seepage analyses to inform engineering design typically adopt a continuum approach

34 with macro-scale parameters. However, the fundamental processes that lead to the internal erosion

35 in embankment dams (ICOLD, 2015) and settlement due to fines migration during dewatering

36 (Preene & Rosser, 2012) initiate at the particle scale. Understanding these processes is important

37 to inform robust approaches to design, e.g. considering whether to continue to use hydraulic

38 gradient rather than seepage velocity when assessing the risk of a seepage-induced instability

39 (Vogt et al., 2015). Incidents such as the failure of Gouhou Dam in 1993 (Zhang & Chen, 2006)

40 and the serious sinkhole incident at WAC Bennett dam in Canada in 1996 (Muir Wood, 2007)

41 remind us of the significant hazard that can be posed by seepage instabilities. Globally, seepage

42 instabilities have caused about 50% of recorded embankment dam failures (Foster et al., 2000).

43 This contribution adopts a combination of particle image velocimetry (PIV) and computational

44 fluid dynamics (CFD) to quantify seepage flow in the void space of a transparent granular soil and

45 to determine the fluid-particle interaction forces that can lead to particle migration and instability.

46   Saturated transparent soils can be created by refractive index (RI) matching between model

47   (analogue) sands formed of borosilicate glass and carefully selected pore fluids. Illumination by a

48   laser light sheet enables visualization of the particles along a plane within the material, and so the

49   internal mechanisms that underlie complex macro-scale behaviours can be studied (Hunter &

50   Bowman, 2018; Iskander et al., 2015). Hunter and Bowman (2018) developed a transparent soil

51   rigid-walled permeameter to study the particle-scale mechanisms that occur during internal erosion

52   in gap graded particulate systems. They considered a single plane within the sample and

53   successfully imaged particle migration. However, there was no local measurement of fluid flow,

54   and the data generated were two-dimensional. Saleh et al. (1992) and Northrup et al. (1993) applied

55   Particle Imaging Velocimetry (PIV) to tracer particles in the pore fluid to generate 2D images of

56   flow in transparent porous media created using RI matching. Peurrung et al. (1995) applied Particle

57   Tracking Velocimetry using a similar experimental set-up, again obtaining 2D data. Alternatively,

58   the flow fields in 2D transparent micromodels fabricated with soft lithography may be determined

59   with micro-PIV (Karadimitriou et al., 2013; Karadimitriou & Hassanizadeh, 2012; Meinhart et al.,

60   1999). However, it is the 3D geometry of the void space that controls flow in the pores; a complete

61   picture cannot be obtained from planar data. 3D flow data can be obtained using tomographic

62   technologies which can be used on opaque materials, e.g. Magnetic Resonance Imaging MRI and

63   Particle Emission Tomography PET (Khalili et al., 1998; Sederman et al., 1997). However, the

64   data generated are often of limited spatial or temporal resolution.

65   Computational fluid dynamics (CFD) has been applied to study flow in porous rocks

66   (Mostaghimi et al., 2013; Nunes et al., 2015; Piller et al., 2014) and in sands (Garcia et al., 2009;

67   Taylor et al., 2016, 2017). In these studies, the topology of the pore space was obtained from

68   micro-computed tomography scans. The volumes of soil/rock considered was relatively small, and

69 ideal flow boundary conditions were typically assumed along the sides of the sample. While the

70 resulting permeabilities appeared reasonable, the accuracy of the velocities within the pores could

71 not be verified, and the implications of the idealized boundary conditions could not be quantified.

72 Huang et al. (2008) and Thaker et al. (2019) determined the 3D topology of the void space in

73 transparent samples, and applied CFD to simulate flow and compared these data with flow field

74 data acquired using PIV. However, the comparisons considered only a single plane and spherical

75 particles.

76   Developing the work of Hunter & Bowman (2018), this study adopts refractive-index-matched

77 transparent materials and PIV to monitor the flow field in a transparent permeameter. A method

78 was developed to precisely control the laser sheet position in order to enable multiple images of

79 the pore topology and the fluid-flow field to be acquired so that, in contrast to earlier studies, quasi-

80 3D experimental data were recorded. Three-dimensional pore topologies reconstructed from slice-

81 by-slice scanning and image processing are incorporated in CFD simulations. This combination of

82 laboratory experiments and numerical modelling enables the following questions to be addressed:

83   i) Can PIV be used to develop a three-dimensional understanding of seepage flow in the void

84   space of granular soils?

85   ii) To what extent do the assumed flow boundary conditions compromise the accuracy of the

86   predictions of the local fluid velocities in CFD analyses of seepage flow in the void space

87   of soil?

88   iii) Particle migration induced by the fluid-particle interaction force initiates all of the

89   instabilities noted above. Can the combined PIV and CFD analyses enable quantification

90   of the fluid-particle interaction forces in real physical systems?

91   In a preliminary application of the approach proposed here, we considered two materials with very

92   different particle morphologies and show how this technique can be used to explore the influence

93   of morphology on flow fields and fluid-particle interaction forces.

94

95   **2. Experimental Setup**

96   *2.1. Transparent soil permeameter*

97   The experimental apparatus is a rigid-walled 'transparent soil' permeameter that has been

98   designed to visualize the mechanisms occurring during seepage-induced internal erosion in

99   susceptible granular media (Hunter & Bowman, 2018). Fig.1 is a sketch of the experimental device.

100   The permeameter is a rectangular cell (100 mm by 100 mm in plan area and 265 mm high). Five

101   vertical manometer ports are arranged at the back of the permeameter for local head measurements.

102   The flow is directed upward via a constant head applied at the base using an adjustable header tank.

103   Flow from the top of the cell is recirculated back into a reservoir and then pumped back into the

104   header tank. A constant head was applied, and the resulting local head values were measured using

105   the manometers located at the back of the permeameter cell. Consideration was restricted to

106   laminar, low Reynolds number flows, typically encountered in geotechnical applications. Particle

107   movement was not expected since the drag forces were relatively low compared with the particle

108   weights (i.e. gravitational force). Also, analysis of the images showed no visible particle movement

109   throughout testing.

2.2. Laser and imaging systems

110

111   A 1.5 mm thick laser sheet parallel to the direction of the flow was applied to the side of the

112   permeameter to illuminate a selected plane perpendicular to the z-axis in Figure 1. The light source

113   was a 1W Kvant continuous wave laser at 520 nm (green) wavelength with variable power control.

114   The laser beam was coupled from the laser head into an optical fibre, recollimated at the fibre

115   output, and then sent through a line generator lens mounted on a lens post and base plate to provide

116   height adjustment. This optical assembly was fixed on a linear micrometre stage with a 25 mm

117   travel range so that specific planes of interest could be imaged and returned to with precision over

118   long-running tests.

119   A high-speed camera, Phantom Miro 310, mounted on another linear micrometre stage with a

120   50 mm travel range was positioned in front of the permeameter cell to record images with a spatial

121   resolution of 1280×800 pixels at 200 frames/s. During each test, the position of the camera in the

122   z-direction was adjusted in accordance with the laser sheet position to retain a sharp image focus.

123   A Nikon AF Nikkor lens 85 mm was used with up to 34 mm of extension rings placed between

124   the lens and the camera sensor. All images were recorded using an aperture f-stop number of 4,

125   which was selected according to its influence on the tracer magnification, as discussed later.

2.3. Tested materials

126

127   Table 1 shows the physical and optical properties of the two model soils. The first sample

128   consisted of 7.5 ± 0.03 mm diameter spherical beads made of borosilicate glass purchased from

129   SiliBeads. The second sample consisted of angular particles made from Duran® glass with size

130   ranging from 6.7 to 9.5 mm (Sanvitale & Bowman, 2012).

131   The particle size was chosen based on a trade-off between different aspects related to the

132   optical technique, practical considerations and standard guidelines. As general rule, the size of the

133   particles must be large enough to ensure the tracers can flow easily through the pores without

134   blocking the channels. In addition, the procedure for Standard Test Method for Permeability of

135   Granular Soils (ASTM D 2434-68, 2000) requires the maximum particle size of the specimen to

136   be 8 to 12 times smaller than the diameter of the permeameter. Furthermore, in previous

137   experimental work (Sanvitale & Bowman, 2012) the same refractive index matched material was

138   used and it was observed that the presence of small particles produces a greater amount of scattered

139   light in the granular system owing to the slight differences in refractive indices at the grain–liquid

140   interfaces. It was found that better transparency even at the deepest illuminated sections, can be

141   obtained when large particles are used. Finally, the availability in the laboratory of a sample of

142   angular particles (that are not commercially available but hand-made, see Sanvitale & Bowman

143   2012) with gradations comparable to those of the beads was taken into account, in order to carry

144   out tests with grains of different shape but compatible drainage behaviour.

145   Each sample was prepared using a 'slurry' placement method to avoid entrapment of air

146   bubbles (Hunter & Bowman, 2018) to create a sample approximately 165 mm in height. In order

147   to develop a uniform pressure and velocity conditions entering the sample, a 45 mm layer of

148   'dispersing' filter material, comprising a mixture of spherical borosilicate beads of 15 mm and 10

149   mm diameter, was placed at the bottom of the apparatus.

150   A hydrocarbon immersion fluid (Cargille Laboratories) was chosen to match the refractive

151   index of the glass particles (Sanvitale & Bowman, 2012; Wiederseiner et al., 2011). As well as a

152   close optical match, the fluid and solid mixture needed to behave similarly to soil and water in

153   terms of buoyancy. The effective specific gravity of the particles compared with the fluid was 2.64

7

154   – which is typical of soil in water. In order to achieve the best refractive index match during testing,

155   different room temperatures were used, 23 °C for the beads and 26 °C for the angular particles.

156   Figure 2(a) shows a typical outcome of refractive index matching under normal lighting conditions.

157   A small amount of Nile Red fluorescent dye, added to the fluid phase, enabled the application of

158   Planar Laser-Induced Fluorescence (PLIF) based imaging on identifying the solid particles with

159   respect to the fluid phase. To characterize the pore topology, the saturated sample was illuminated

160   by the laser sheet whose wavelength matched the absorption peak of the fluorescent dye within

161   the fluid. The resulting fluorescence (where the dye emits light at a wavelength greater than that

162   of the excitation wavelength) was recorded by the high-speed camera through a long-pass filter

163   placed over the lens to transmit only the fluorescence signal and discard the green laser light: the

164   particles show as dark on a bright fluid background.

165

166   **3. Particle Image Velocimetry (PIV) Analyses**

167   *3.1. Calibration for image size and distortion*

168   Before each test, the image size and distortion were calibrated with fixed grid dots at 1 mm ±

169   0.001 mm spacing inside the permeameter cell filled with the liquid phase at the locations of the

170   26 vertical planes imaged in the experiment. The distortion error due to the optical assembly was

171   corrected according to the procedure discussed in Gollin et al. (2017). The coordinates of the dots

172   were estimated with sub-pixel accuracy and associated with an undistorted grid and then

173   interpolated using a built-in MATLAB function Scattered-Interpolant (Brevis et al., 2011). This

174   approach adopts a linear interpolation based on Delaunay triangulation.

175　*3.2. Seed tracers*

176　　　The fluid flow field was imaged using reflective seed tracers dispersed in the liquid phase.

177　These seeding particles should be neutrally buoyant and small enough to follow the flow accurately.

178　Silver-coated hollow microspheres with a nominal size ranging between 5-30 µm were used at a

179　concentration of 35 mg/l. These had a density of 0.75 g/cm^3, resulting in an effective specific

180　gravity of 1.13 compared to the fluid, i.e. close to unity. To ensure that the inertia effects due to

181　particle density were negligible so that the tracers would reliably follow the flow, the Stokes

182　number was calculated as follows:

$$Stk_s = \frac{\rho_s d_s^2 u_y}{18 v \rho D} \ll 1 \qquad \text{(Eq. 1)}$$

183　where d_s and ρ_s are the seed diameter and density, respectively, D the bead diameter, v and ρ the

184　fluid kinematic viscosity and density, respectively, and u_y is the axial (y-direction) fluid velocity

185　of the flow. For our set-up, the maximum Stokes number was calculated to be Stk_s= 2.59 x 10^{-6}.

186　The movement of the tracers was recorded by removing the long-pass filter in front of the camera

187　lens to allow the light reflected from their surfaces to be captured. Figure 2(b) and (c) show how

188　laser illumination enables internal visualization of a plane within both spherical bead and angular

189　particle samples with the tracers. Two videos, V1 and V2 in the supplementary material, show the

190　movement of tracers in both spherical bead and angular particle samples. Figure 2(d) shows the

191　top view of the laser sheet illuminated plane with a finite thickness of around 1.5 mm.

192　*3.3. Image acquisition for 3D volumes*

193　　　The flow fields inside two 3D volumes were examined within each sample. The lower volumes

194　were located between manometer ports P2 and P3 and denoted as sub-volumes Beads-L and Ang-

195　L for the spherical sample and angular samples, respectively (Figure 1). The upper volumes were

196　located between manometer ports P3 and P4 and denoted as sub-volumes Beads-U and Ang-U,

197　respectively. The dimensions of sub-volumes varied slightly with the position of the high-speed

198　camera, as shown in Table 2. In each sub-volume, the flow fields on 26 planes parallel to the flow

199　directions were measured. These planes were evenly spaced at 1 mm ±0.001mm, centred in the

200　mid-section of the permeameter cell with at least 32 mm distance from the lateral sidewalls. The

201　choice of inter-plane spacing was made based on the laser sheet thickness of 1.5 mm. On each

202　plane, a series of images were taken over 2 seconds at 200 frames/s, i.e. 400 images were taken

203　per plane.

204　*3.4. PIV postprocessing*

205　　An open-source software, PIVlab (Thielicke & Stamhuis, 2014), was used for image

206　processing to determine the flow velocities. PIVlab gives an Eulerian description of the

207　investigated velocity field, estimating the displacement for groups of tracers by determining the

208　peak of the cross-correlation of many small interrogation areas. This software uses a multi-pass

209　cross-correlation algorithm coupled with a window deformation technique to obtain the velocity

210　vectors (Thielicke, 2014). The 2-step correlation algorithm with decreasing window size (D_I) was

211　used to evaluate the recorded images with a final size of 32×32 pixels (approximately 1×1 mm^2

212　area), set to minimize the loss of in-plane particle pairs ensuring that the x and y displacements

213　were smaller than DI/4. The loss of particle pairs between corresponding interrogation windows

214　due to out-of-plane motion was limited due to the fact that the *z* displacement of the tracer particles,

215　which can be assumed to be of the same magnitude as the tracer particle displacement in the *x*-

216   direction, was less than a quarter of the light sheet thickness (Atkins, 2016; Keane & Adrian, 1993).

217   The overlap of the interrogation windows was 50% for all steps.

218   The velocity fields for each plane position were calculated by averaging over 2 s of recorded

219   images, and the 'instantaneous velocities' were estimated on two successive frames separated by

220   a time steps Δt. The frame rate was 200 fps for all of the experiments. The influence of the time

221   step on the fluid velocities was studied by setting Δt equal to 5, 10, 20 and 40 ms, equivalent to 1,

222   2, 4 and 8 frames (Figure S1 is provided as supplemental material). Decreasing Δt from 40 to 10

223   ms caused an increase in the time-averaged u_y and u_x values. Further decreasing Δt from 10 to 5

224   ms led to little variation in either u_y or u_x, meaning the true maxima of velocity were captured at a

225   time step of around 10 ms. Therefore, a time step Δt of 10 ms was chosen for the PIV analyses to

226   avoid positional errors associated with reducing the time step to very low values (Gollin et al.,

227   2017).

228   The seeding density was approximately five tracers inside an interrogation window for both

229   tests (as shown in Figure S2 in the supplemental material) which is within the optimal range to

230   achieve a successful correlation and minimum random error (Thielicke, 2014). The seed image

231   size d_τ was estimated as the width of the autocorrelation peak of a typical set of interrogation

232   windows (Michaelis et al., 2016; Patil & Liburdy, 2013). The autocorrelation peak width was

233   calculated using the e^{-2} width. The resulting widths were 3.57±0.72 pixels for the test with the

234   spherical beads and 3.27±0.81 pixels for the test with angular particles (Figure S3). Both sizes lie

235   in the range of the tracer image diameter to achieve optimal measurements using the window

236   deformation algorithms in PIVlab (Thielicke, 2014).

3.5. Boundary flow field on a single plane

238   Figure 3 shows a typical flow field across the whole permeameter for a sample of beads,

239   considering three sub-volumes in the left, middle and right, respectively. The PIV analyses

240   performed here show how the rigid lateral boundaries of the permeameter can disrupt the particle

241   packing, leading to some areas of large flow velocity in comparison to the mean, for example with

242   the high flow at the left boundary of Figure 3(a) compared to (b) and (c). In this preliminary

243   examination of the flow, an image mask was manually applied to the particle positions to exclude

244   them from the fluid flow analysis. In contrast, for the following analyses focused on volumes at

245   the centre of the permeameter, the masks were automatically determined from image processing.

246

247   **4.   Image Processing**

248   *4.1. Image segmentation*

249   Figure 4(a) shows a typical grey-scale image of a plane from sample Beads-U, illuminated by

250   the laser. As shown in the schematic diagram at the top of the image, the finite laser thickness

251   leads to non-uniform grey values because particles can partially fill the laser beam. This is similar

252   to the partial volume effect associated with microCT images and consequences for image quality

253   are related to the laser thickness. The histogram of grey values of the image as shown in Figure

254   4(b) indicates there is no clear separation between the grey values for the particles and the pore-

255   space. The distance between the scanning planes determines the image resolution in the z-direction,

256   i.e. the effective voxel length in the z-direction is 1 mm. Furthermore, the laser sheet creates linear

257   streaks or shadows in the direction of the laser, with grey values that can be similar to that of

258   particles. In previous studies, the 3D pore space was reconstructed by identifying the centre and

259 radius of each spherical particle from 2D slices (Huang et al., 2008; Thaker et al., 2019) rather

260 than considering the 3D dataset directly. This shape-matching approach cannot be used for samples

261 with irregular-shaped particles.

262 Image segmentation of granular materials classifies each pixel as being either within a particle

263 or within the pore-space. We explored three approaches to segment the images, and Figure 5

264 presents the results of each of these methods applied to three representative slices. The first

265 approach is threshold segmentation which classifies all pixels with a grey value lower than a

266 specified threshold as being in the particle phase and the remaining in the pore phase. The threshold

267 can be automatically determined by Otsu's algorithm based on the grey value histogram, as shown

268 in Figure 4(b) (Otsu, 1979). The Otsu-threshold segmentation method incorrectly classified some

269 linear shadows created by the laser as being in the particle phase.

270 The other two methods considered, namely the trainable Weka (Waikato Environment for

271 Knowledge Analysis, Arganda-Carreras et al., 2017) and the U-Net (Ronneberger et al., 2015), are

272 based on artificial intelligence. Artificial intelligence segmentation approaches learn from

273 manually segmented images to define a pixel-wise classifier which labels each pixel as being in

274 either the particle or pore phase. The trainable Weka algorithm was developed in the open-source

275 software platform Fiji (Schindelin et al., 2012). When compared with the Otsu threshold, this

276 method improved the segmentation quality to some extent, but it could not completely remove the

277 laser-induced linear shadows. Finally, the U-Net algorithm proved to be more robust in

278 segmentation, producing smooth particle-pore interfaces and no linear shadows, in contrast with

279 the other two methods. The segmented results from U-Net have smooth particle surfaces, no

280 internal voids in the particles and eliminate all linear artefacts induced by the laser, which is

281 important for constructing CFD models. U-Net performs segmentation based on both grey values

13

282 and morphological patterns, e.g., edges, curvatures, and spheres. The U-Net package was

283 implemented in Tensorflow and Keras following the U-Net architecture proposed by Ronneberger

284 et al. (2015).

285 The U-Net segmentation procedure can be divided into three major steps: (a) data preparation

286 for training; (b) U-Net training; and (c) new image segmentation (Figure 6). The U-Net

287 architecture requires an image dimension of 512×512. Therefore, the images were scaled from

288 1280×800 pixels to 512×512 pixels and scaled back after segmentation. Initially, eight images

289 were segmented by visual inspection. Data augmentation was performed to increase the diversity

290 of training data by shifting and rotating each annotated image to produce four images. Thus a total

291 of 32 images were obtained for training and validation. Then the U-Net algorithm was trained with

292 32 annotated images to define the classifier. The trained U-Net classification led to an accuracy of

293 about 93% for validation images and was used as a classifier to segment new images. The U-Net

294 classification generated a grey-scale image in which the grey value of a pixel reflected the

295 possibility of that pixel being in a particle. A target porosity was specified to generate an

296 appropriate threshold grey-level value to binarize the output of the U-Net algorithm. This porosity

297 was selected by considering the experimental whole-sample value. However, acknowledging the

298 sample heterogeneity, a parametric study was carried out considering a range of reasonable local

299 porosity values as discussed below.

300 *4.2. Three-dimensional pore structure reconstruction*

301 The slice-by-slice scanning method led to an in-plane pixel size of approximately 0.029 mm

302 along the x- and y-axes, and an out-of-plane distance of 1 mm along the z-axis. Therefore, we

303 applied a scaling to the output from U-Net to reconstruct a three-dimensional volume with an

14

304 identical voxel size of 0.1 mm along all directions. Figure 7 shows the effect of upscaling along

305 the *z*-direction with three different interpolation methods. The scaling without interpolation results

306 in a stepped particle surface, while both interpolation methods provide relatively smooth particle

307 surfaces. The bilinear interpolation is adopted in this study. Finally, we binarized the scaled three-

308 dimensional images with a threshold value to reach the porosity value determined experimentally.

309 The threshold value was determined from the linear relationship between the threshold value and

310 the resulting porosity. Three levels of porosity were used to reconstruct the pore topology to

311 investigate the influence of porosity on the CFD results.

312   We performed marker-based watershed labelling to identify individual particles from three-

313 dimensional binary images. The image processing steps involved in labelling particles are: (a)

314 construct a distance map representing the distance from a pixel to its closest particle surface; (b)

315 use marker identification based on the H-Maximum algorithm (Soille, 2013) on the distance map;

316 (c) implement marker-based watershed segmentation using the markers and distance map. A more

317 detailed description of this marker-based watershed segmentation approach can be found in Zhao

318 et al. (2015). Figure 8 illustrates the labelling results on typical 2D slices for beads and angular

319 particles. The particles are less regular on x-z planes than on x-y planes. This is mainly due to the

320 finite step distance during the slice-by-slice scanning along the z-axis.

321   A marching cubes algorithm was used to generate triangular surface meshes from the voxel

322 assembly representing individual particles (Lorensen & Cline, 1987). The surface meshes of

323 individual particles were cleaned, simplified and smoothed with GMSH, an open-source mesh

324 generator (Geuzaine & Remacle, 2009). Finally, the surface meshes of all particles were combined

325 into a single file with individual particles represented by a unique label. Figure 9(a) and (b) show

326   the three-dimensional views of the particle packings in the scanning region for the samples with

327   spherical beads and angular particles, respectively.

328

329   **5. Computed Fluid Dynamics (CFD) Simulation**

330   *5.1. Governing equation and numerical method*

331   For the fully saturated conditions assumed here, flow through the pore space is governed by

332   the incompressible Navier-Stokes equations formulated as:

$$\rho_f \left(\frac{\partial \boldsymbol{u}}{\partial t} + \boldsymbol{u} \cdot \nabla \boldsymbol{u} \right) = -\nabla p + \mu \nabla^2 \boldsymbol{u} \qquad \text{(Eq. 1)}$$

$$\nabla \cdot \boldsymbol{u} = 0 \qquad \text{(Eq. 2)}$$

333   where $\boldsymbol{u}$ is the velocity vector, and p is the pressure. In the steady-state, $\partial \boldsymbol{u}/\partial t = 0$. Here the

334   Navier-Stokes equations were solved using the Semi-Implicit Method of Pressure Linked

335   Equations (SIMPLE) algorithm in the open-source CFD toolbox OpenFOAM (OpenFOAM

336   Foundation, 2019). The SIMPLE algorithm is a steady-state solver for incompressible flow. The

337   CFD analysis provides the velocity and pressure values at the centre of each CFD cell.

338   The simulation domain was discretized by the mesh generation algorithms available in

339   OpenFOAM, i.e., BlockMesh and SnappyHexMesh. BlockMesh decomposes the simulation

340   domain into blocks, while SnappyHexMesh takes the surface mesh defining the pore structure and

341   chisels it with the geometry defined by the combined surface mesh file. We applied localized

342   refinement at the particle surface, which increased the mesh densities close to the particle-particle

343   contacts in particular. This created CFD meshes with around 3.5 million cells. Figure 9(c) and (d)

344   show typical CFD meshes of pore space for spherical beads and angular particles, respectively.

345   In all simulations, a constant pressure boundary condition was applied at both the inlet (17 Pa)

346   and outlet boundaries (0 Pa). A 'slip' condition was applied to the four lateral boundaries so that

347   the velocity component normal to each of these boundaries was set to be zero while the tangential

348   velocities remained unconstrained. A 'no-slip' boundary condition was applied to the particle

349   surfaces so that the velocities normal and tangential to the surface were set to zero. These boundary

350   conditions are similar to those applied in the CFD analyses by Taylor et al. (2016). They do not

351   capture the heterogeneity of the pressure and velocity distributions that exist on the boundaries of

352   sub-volumes in experiments. However, the flow velocity data available from the experiments are

353   restricted to 2D and limited to 26 discrete vertical planes. A valid CFD analysis requires

354   conservation of mass (adherence to continuity) in the model in all three dimensions. Consequently,

355   it was not possible to use the experimental data to apply non-uniform velocity fields along the

356   boundary to the simulation domain.

357   The normal and shear stresses on the particle surface were determined from the flow velocity

358   and pressure fields. Each particle surface was discretized into surface elements. Then, the flow-

359   induced force and moment on individual particles were calculated by integrating normal pressure

360   and viscous shear stresses over all elements on the particle surface:

$$\boldsymbol{F_p} = \sum_{i=1}^{N_e} \rho p_i A_i \boldsymbol{n}_i \qquad \text{(Eq. 3)}$$

$$\boldsymbol{F_v} = \sum_{i=1}^{N_e} \mu \boldsymbol{R}_{dev} A_i \qquad \text{(Eq. 4)}$$

361   where N_e is the number of elements covering the particle surface, ρ is the fluid density, p_i is the

362   kinematic normal pressure, A_i and $\boldsymbol{n}_i$ are the patch area and normal vector, μ is the fluid dynamic

363   viscosity, and $\boldsymbol{R}_{dev}$ is the deviatoric stress tensor. The integration was performed using the in-built

364   function, 'forces', in OpenFOAM (OpenFOAM Foundation, 2019).

5.2. Validation with regular packings

366   The CFD simulation data are inherently dependant on the mesh density (cell size) (e.g. Knight

367   et al. 2020). The sensitivity of the fluid-particle interaction forces obtained from the CFD

368   modelling approach adopted here to the mesh density was examined by considering the data in

369   Zick & Homsy (1982) for simple cubic (SC) and face-centred cubic (FCC) packings of uniformly

370   sized spheres. Following Knight et al (2020), the models exploited geometric symmetry to reduce

371   the calculation cost. As before, a specified pressure was applied at the inlet and outlet, while 'cyclic'

372   boundary conditions were applied to the four lateral boundaries. The sphere centroids were placed

373   on a fixed lattice, and the particle sizes were changed to reach different packing densities; e.g. the

374   particle diameter was increased from 4.4 mm to 4.9 mm in the FCC packings to achieve porosity

375   between 0.495 and 0.303. The fluid-particle interaction coefficient, $\bar{F}_{f \to s}$, is the fluid-particle

376   interaction force normalized by Stokes drag force $F_{f \to s}^{s}$:

$$F_{f \to s}^{s} = 3\pi\mu D |u| \qquad \text{(Eq. 5)}$$

$$\bar{F}_{f \to s} = F_{f \to s} / F_{f \to s}^{s} \qquad \text{(Eq. 6)}$$

377   where D is the particle diameter, u is the superficial flow velocity, and $F_{f \to s}$ is the fluid-particle

378   interaction force, which includes both the pressure and viscous terms.

379   The fluid-particle interaction coefficient increases with reduced packing porosity, as shown in

380   Figure 10(a). The results from CFD simulations are consistent with the Zick and Homsy solutions

381   and the results from Immersed Boundary Method (IBM) obtained by Knight et al. (2020). The

18

382   CFD results are mesh dependent. As shown in Figure 10(b) and (c), the agreement between the

383   fluid-particle interactions obtained from these CFD simulations and the Zick and Homsy data,

384      $|\bar{F}_{f \to s} - \bar{F}_{f \to s}^{ZH}|/\bar{F}_{f \to s}^{ZH}$, improves with increasing mesh density, D/d_m, where D is the particle

385   diameter, and d_m is a characteristic mesh element size. At the same D/d_m, the relative error

386   increases with sample density. The relative errors for most samples were smaller than 5% at a D/d_m

387   of 40. The results obtained from the unstructured mesh CFD analyses by Knight et al. (2020) show

388   a similar influence of mesh density on relative error for drag estimation. The average ratio between

389   particle diameter and mesh element size was chosen to be 40 for the permeameter simulations.

390

391   **6. Results**

392   The 2D-PIV measurements can only provide the components of flow velocities in the plane of

393   the laser, i.e. along the x- and y-directions. Within this plane, the distance between PIV data points

394   is around 0.5 mm, which is much larger than the CFD mesh size. Therefore, the CFD velocity

395   fields were interpolated to the centre of the PIV interrogation regions to allow a direct comparison

396   between the PIV and CFD results. The Reynolds number in this study is around one, which

397   indicates a laminar flow condition. We normalized the velocity values by the mean vertical

398   velocity either on each vertical slice ($\bar{u}^s$) or the mean value in each sub-volume ($\bar{u}^v$).

399   For each sub-volume, the PIV analysis was performed on 26 x-y planes at 1 mm intervals. The

400   x-y planes were referred with their z coordinates from 0 mm to 25 mm. The CFD domain is slightly

401   smaller than the PIV domain and has 24 x-y planes (z = 1 to 24 mm) to reduce the effects of

402   upscaling on boundary slices (Figure 7). The sub-volume has about six particles along the x-

403   direction and four particles along the y-direction, and there are about 20 particles completely inside

404   each sub-volume.

6.1. Permeability estimation

406   Table 3 shows the experimental measurements for each sub-volume. Each sub-volume is

407 named by the particle type, e.g. spherical (Beads) and angular (Ang), followed by the position, e.g.

408 upper (U) and lower (L). The overall packing porosity, n, permeameter cross-section area, A_{Exp},

409 and flow rate, Q_{Exp}, were measured during each permeameter test. Local manometer readings were

410 used to identify the hydraulic gradient for the experiments, and the two sub-volumes in the angular

411 particle sample had slightly different hydraulic gradients i_{exp} due to the inhomogeneous packing.

412 Seepage flow rates were determined from experimental measurements (u_{seep}^{Exp}), PIV analysis (u_{seep}^{PIV})

413 and CFD simulations (u_{Seep}^{CFD}).

414   Figure 11 compares the permeability values estimated by the three types of seepage velocities.

415 In general, the permeability values estimated by PIV analysis (k^{PIV}) are smaller than the values

416 estimated from the experimental measurements (k^{Exp}). This is unsurprising as the PIV analysis

417 was performed over central sub-volumes, while the pump injection rate measures the cross-section

418 of the permeameter, including the larger voids commonly encountered at the side walls (Figure 3).

419 In addition, the sub-volumes for Ang show smaller permeabilities than the sub-volumes for Beads.

420 For k^{Exp} the sub-volume Ang-U has a higher permeability than for Ang-L due to the different

421 hydraulic gradient as measured using the manometers, while there was no evident difference in the

422 sub-volumes of the Beads sample. In Figure 11(a) the k^{CFD} data were obtained using the overall

423 experimental porosities, i.e. n= 0.38 and 0.36 in the CFD simulations for Beads and Ang samples,

424 respectively. Perhaps surprisingly, the permeability values estimated by CFD simulations, k^{CFD}

425 (grey data points), are similar across the four sub-volumes, with only a slight decrease for the Ang

426 sample compared to the Beads. This means that, while the permeabilities estimated for CFD and

427   PIV in the Beads sub-volumes are quite close, for the angular sample, k^{CFD} measurements are

428   approximately twice that of k^{PIV}.

429   The differences between experimental and numerical permeabilities could be caused by (a)

430   local porosity variations, (b) CFD boundary effects, or (c) PIV velocity measurement errors. Figure

431   11(b) illustrates the sensitivity of the k^{CFD} results to porosity by considering three limiting

432   plausible porosity values. For Beads-U, k^{CFD} agrees with both k^{Exp} and k^{PIV} if local porosity is

433   changed from 0.38 to 0.40. For Ang-U, k^{CFD} agrees with k^{Exp} and k^{PIV} if the local porosity is

434   changed from 0.36 to 0.31 and 0.29, respectively. However, the segmented images seem to be

435   inconsistent with the grey-value images due to the large porosity change (Figure S4 in the

436   supplementary material). Furthermore, the variation in porosity had only a limited influence on the

437   flow field distributions. Potential PIV velocity measurement errors were also investigated by

438   changing the framerate. However, this did not lead to a noticeable change. A definitive, precise

439   explanation for the inconsistency in the permeability values could not be determined.

440   *6.2. Flow fields – contour plots*

441   The normalized flow fields obtained from PIV and CFD analysis within a typical x-y plane for

442   the Beads-U sub-volume are in good agreement, as shown by the normalized horizontal velocity

443     $\bar{u}_x^s$ and vertical velocity $\bar{u}_y^s$ in Figure 12. The heterogeneity in the packing leads to concentrated

444   flow paths for vertical flow at some large voids, e.g. close to the left bottom corner. The horizontal

445   velocity is determined by the local pore alignment relative to the macro-scale flow direction. The

446   lateral boundaries assumed in the CFD models prohibit horizontal flow, so the flow patterns at the

447   side boundaries differ. For example, the physical test data indicate a relatively large horizontal

448   flow close the left boundary in Figure 12(a) which is not captured in the CFD model in Figure

449   12(b). The difference in the boundary conditions also influences the vertical velocity values in this

450   region. The vector plots of flow fields on three x-y planes are shown in Figure 13 to further

451   demonstrate the similar patterns revealed by PIV and CFD estimations. Again, the lateral boundary

452   conditions inhibit horizontal flow in the CFD model.

453   The flow velocities on four x-y planes in the Beads-U sub-volume were analysed statistically,

454   as shown in Figure 14. The horizontal normalised velocity $\bar{u}_x^s$ tends to form a Laplace distribution

455   with a mean velocity around zero (Figure 14(a)). While the distributions obtained from the PIV

456   analyses are similar for the four planes considered, the two CFD distributions with z= 1 mm and

457   24 mm tend to have a higher proportion of data points with a velocity close to zero, due to the

458   lateral boundary effect experienced at the front (z = 1 mm) and back (z = 24 mm) of the studied

459   volume. The vertical normalised velocity $\bar{u}_y^s$ tends to form a half Laplace distribution (Figure

460   14(b)). Similarly, the planes close to the front or back lateral boundary in the CFD simulation (z=

461   1 mm and 24 mm) have a higher proportion of velocity close to zero. The cumulative distributions

462   in Figure 14(c) and (d) show a good agreement between PIV and CFD results.

463   The pore topology is intrinsically correlated with particle morphology and granular material

464   packing/fabric. The flow fields on three x-y planes of the Ang-L sub-volume show the flow

465   patterns that are distinct from those developed in the Beads-U sub-volume (comparison between

466   Figure 15 and Figure 13). Some flow channels are straight rather than converging-diverging due

467   to the flat surfaces of angular particles, as indicated by arrows. The difference seems to be more

468   obvious for the angular particle sample than for the beads sample. However, the overall

469   distribution of flow velocity in the angular particles sample is very similar to that of the beads

470   sample, as shown in Figure 16. Previous studies have indicated that the flow velocity distribution

471 depends on packing density (Rong et al., 2013). Further tests are needed to investigate the influence

472 of particle shape on the flow velocity distribution.

473 　　The mapping of the CFD data onto the PIV grid allows spatial variation of the difference

474 between the two datasets to be examined, as shown in Figure 17(a) and (b). While the data in

475 Figure 12 showed the similarity of the flow patterns, there are large differences between the

476 normalized velocity intensities. Figure 17(c) and (d) show the cumulative distributions of the

477 velocity difference values for five x-y planes. The difference mainly lies between $\pm 50\%$ and

478 $\pm 100\%$ of the mean seepage velocity on each slice for horizontal and vertical velocity,

479 respectively. Perhaps unsurprisingly, the planes closest to the lateral boundaries (z= 1 or 24 mm)

480 have a higher velocity difference.

481 *6.3. Mean flow rate on slices*

482 　　Here, the mean velocity on each x-y plane is normalized by the seepage velocity in each sub-

483 volume. The normalized vertical velocity on each plane varies between 0.5 and 1.5, as shown by

484 Figure 18(a). The PIV and CFD data exhibit similar patterns of variation in $\langle \bar{u}_y^v \rangle$ along the z-axis.

485 In the CFD analyses, the lateral boundaries prohibit out-of-plane flow and lead to low velocity

486 values along z, as shown by the shaded area in Figure 18(b). However, $\langle \bar{u}_z^v \rangle$ increases to the

487 expected level after about 3 mm (~D/2) from the lateral boundary. The heterogeneity of the pore

488 structure and relatively small sub-volume leads to a large variance of the plane-based porosity

489 (Figure 18(c)). For example, the plane-based porosity for the Beads-U sub-volume (n= 0.38) varies

490 from 0.25 to 0.5.

491 　　The CFD analyses provide 3D data, enabling analysis of the velocity distribution in horizontal

492 x-z planes perpendicular to the flow direction. As expected, the variance of the mean vertical

23

493   velocity $\langle \bar{u}_y^v \rangle$ on x-z planes is inversely correlated to the plane porosity due to the fluid continuity

494   (Figure 19(a) and (b)). Where the porosity in the x-z plane is lower, $\langle \bar{u}_y^v \rangle$ is higher so that overall

495   flow rate is the same for each x-z plane in line with the principle of mass conservation. The pressure

496   dissipation is higher at the lower porosity plane, as shown in Figure 19(c).

497   *6.4. Fluid-particle interactions*

498   Each sub-volume contains around twenty particles that do not intersect the boundaries. Figure

499   20 shows the vector plots of the fluid-particle interaction coefficients $\bar{F}_{f \to s}$ (Equation 6) projected

500   onto x-y planes for four sub-volumes. The magnitudes of $\bar{F}_{f \to s}$ have a large variance, especially

501   for angular particles. The directions of $\bar{F}_{f \to s}$ slightly deviate from the flow direction – the mean

502   deviation angle equals 16°. The variance of $\bar{F}_{f \to s}$ arises mainly from the heterogeneous flow fields,

503   resulting from local packing and irregular particle morphologies.

504   Figure 21(a) shows the distribution of the fluid-particle interaction coefficient, which varies

505   approximately from 50 to 140 for beads and from 50 to 240 for angular particles. The mean value

506   of $\bar{F}_{f \to s}$ is influenced by the different packing densities, with the angular particle sample having a

507   slightly higher packing density than the beads sample. Figure 21(b) shows the fluid-particle

508   interaction coefficients normalized by their mean values. Clearly, the sample with angular particles

509   has a higher variance than the spherical beads sample. This variance may arise from packing

510   density or particle shape difference.

511   The fluid-particle interaction is contributed by two components, i.e. a viscous component due

512   to skin friction and a pressure component due to the pressure gradient. In dense packings, the

513   pressure component of fluid-particle interactions dominates the fluid-particle interaction, while the

514   viscous component accounts for about 20% on average, as shown in Figure 22(a). Spherical beads

515   tend to experience a slightly higher ratio of the viscous component to pressure component than

516   angular particles. Figure 22(b) shows the deviation angle of fluid-particle interactions from the

517   flow direction, i.e. $\theta_d = \arctan(\bar{F}_{f \to s, xz}/\bar{F}_{f \to s, y})$. Most particles have a deviation angle between $0°$

518   and $30°$.

519

520   **7. Conclusions**

521   This study investigated pore-scale seepage in granular packings with the combined

522   experimental and numerical methods. Permeameter tests were performed with transparent soils

523   consisting of spherical and angular particles. PIV analysis quantified 2D flow fields inside granular

524   packings on multiple planes. We adopted a series of image processing techniques to reconstruct

525   the 3D pore topologies from the slice-by-slice scanning images. Pore-scale CFD analysis was

526   performed on reconstructed volumes to obtain both flow fields and fluid-particle interactions. The

527   fluid-particle interactions obtained by CFD simulations were validated with existing results on

528   regular particle packings. The conclusions are summarised as follows.

529   PIV analysis can quantify the flow field for two-dimensional planes. The random packing of

530   particles leads to preferential flow paths at larger voids (e.g. close to boundary wall). Spherical

531   particles tend to form converging and diverging flow paths, while angular particles with flat

532   surfaces form straight channels. The interplays between local particle arrangement, particle shape

533   and pressure gradient determine the heterogeneous pore-scale flow fields.

534   The slice-by-slice images containing pore structure information were obtained by illuminating

535   the transparent soils at multiple locations with a sheet laser. An artificial intelligence algorithm

536   provided good image segmentation results for the images with poor contrast and artefacts. The

537   flow fields obtained from CFD analysis on the reconstructed pore structure show a good agreement

538   with PIV results. Similar patterns were obtained for the contour plots of flow fields, flow vector

539   plots and velocity magnitude histograms. This agreement demonstrates the successful

540   implementation of the three-dimensional pore structure reconstruction methods. However, while

541   there is good agreement between the average flow fields, the local differences in flow field data

542   are more significant.

543   This work supports the development of systems with thinner lasers (including the requisite

544   safety considerations) and exploiting recent advances in automated systems for macro photography

545   to reduce the observed partial volume effects and improve the resolution orthogonal to the

546   scanning planes (i.e. in the z-direction considered here).

547   The CFD results have a higher resolution in comparison with the PIV results and produce

548   three-dimensional velocity values. However, the analyses tend to have side boundary effects. The

549   comparison between CFD and PIV results indicate the side boundary effects are usually

550   constrained within a half particle diameter region. The point-by-point comparison of CFD and PIV

551   results was performed after downscaling the CFD results. The normalized velocity difference

552   remains large, even though the overall distribution of CFD and PIV flow fields are similar.

553   The fluid-particle interactions obtained from fully resolved CFD analysis are consistent with

554   previous numerical solutions. The fluid-particle interactions obtained the permeameter model tests

555   have a large variance, especially for angular particles. For relatively dense packings, viscous drag

556   contributes to a small fraction of the total fluid-particle interaction. The fluid-particle interaction

557   slightly deviates from the injection direction. However, for this study, the number of particles in

558   each CFD model was relatively small (around twenty), and the beads and angular particles samples

559   have slightly different packing density. Therefore, the fluid-particle interaction results should be

560   further investigated to elaborate on the particle shape effects.

List of Figure and Table Captions

561

562   Figure 1. Schematic of the experimental set up.

563   Figure 2. Images of experimental setup: (a) Permeameter cell partially filled with oil; (b) Beads

564   sample illuminated by laser sheet; (c) Angular particles sample illuminated by laser sheet; (d)

565   top view of the laser sheet.

566   Figure 3. Flow fields in the (a) left, (b) middle and (c) right for the permeameter with beads.

567   Figure 4. (a) Typical grey-scale image in Beads-U sub-volume, $z = 0$ mm. (b) Histogram of grey

568   values. Inset in (a) shows that the non-uniform intensity is a consequence of the finite laser

569   width.

570   Figure 5. Segmentation results for three typical slices in Beads-U sub-volume using three different

571   segmentation methods: threshold segmentation with Otsu's threshold, trainable Weka

572   segmentation, and U-Net segmentation. Note: ~~red~~ dashed circles indicate the artifacts produced

573   by inaccurate segmentation.

574   Figure 6. U-Net segmentation procedure for Beads-U sub-volume: (a) Step-1: prepare training and

575   validating data sets; (b) Step-2: train U-Net algorithm; (c) Step-3: apply trained U-Net as a

576   classifier for segmenting new images.

577   Figure 7. Upscaling along z-direction on the U-Net classified image for Beads-U sub-volume: (a)

578   Unscaled image data; (b) Image obtained by scaling without interpolation; (c) Image obtained

579   by scaling with bilinear interpolation; (d) Image obtained by scaling with bicubic interpolation.

580   Figure 8. Labelled images with particles represented by different colours for Beads-U sub-volume

581   on (a) x-y plane and (b) x-z plane and Ang-U sub-volume on (c) x-y plane and (d) x-z plane.

582   Figure 9. Three-dimensional views of the combined surface meshes for (a) Beads-U sub-volume

583   and (b) Ang-U sub-volume. Note: colour is used to distinguish the surfaces of individual

584   particles. Hexahedron meshes which discretize pore structure for CFD simulation for (c)

585   Beads-U sub-volume and (d) Ang-U sub-volume.

586 Figure 10. Verification of CFD modelling approach: (a) Confirmation of ability to capture the

587   influence of porosity on the fluid-particle interaction coefficient $\bar{F}_{f \to s}$, dashed lines indicate a

588   curve fit to the Zick & Homsy (1982) data; (b) Mesh dependence of $\bar{F}_{f \to s}$ for SC packings; (c)

589   Mesh dependence of $\bar{F}_{f \to s}$ for FCC packings. The results predicted by the Immersed Boundary

590   Method (IBM) with a regular grid and from fully resolved CFD using an unstructured meshes

591   from Knight et al. (2020) are included in (a) and (c), respectively.

592 Figure 11. (a) Hydraulic permeability values predicted by experiments, PIV and CFD

593   measurements. (b) Influence of porosity on hydraulic permeability as estimated by CFD

594   modelling for Beads-U and Ang-U sub-volumes. The prediction results from Kozeny-Carman

595   Equation (KC Eq.) is included in (b).

596 Figure 12. Comparison of the PIV and CFD flow fields in Beads-U sub-volume on the vertical

597   slice with $z = 16$ mm.

598 Figure 13. Comparison of the PIV and CFD flow fields in Beads-U sub-volume on three slices

599   with $z = 1, 8$ and 16 mm. Velocity vector length is normalized by seepage velocity.

600 Figure 14. Cumulative distributions of flow velocity at four vertical planes in Beads-U sub-volume

601   obtained from PIV and CFD results.

602 Figure 15. Comparison of the PIV and CFD flow fields in Ang-L sub-volume on three slices with

603      $z = 1, 8$ and 16 mm. Velocity vector length is normalized by seepage velocity. Arrows indicate

604   narrow flow paths.

605 Figure 16. Cumulative distributions of flow velocity at four vertical planes in Ang-L sub-volume

606   obtained from PIV and CFD results.

607   Figure 17. Difference between PIV and CFD flow fields for the vertical slice with z = 16 mm in

608   Beads-U sub-volume: (a) horizontal velocity; (b) vertical velocity. The cumulative

609   distributions of PIV and CFD difference for (c) horizontal velocity and (d) vertical velocity on

610   five typical slices in Beads-U sub-volume.

611   Figure 18. Variation of the mean velocity values obtained from PIV and CFD results and the slice

612   porosity on x-y planes parallel to flow direction.

613   Figure 19. Variation of mean vertical velocity, porosity and hydraulic gradient on x-z planes

614   perpendicular to flow direction predicted by CFD simulations.

615   Figure 20. Projection views of drag force vectors for the particles that are not intersecting with

616   boundary walls.

617   Figure 21. Cumulative distributions of (a) fluid-particle interaction coefficients for beads and

618   angular particles and (b) the normalized fluid-particle interaction coefficients.

619   Figure 22. Distributions of (a) the ratio between pressure and viscous drag components, and (b)

620   the angle between fluid-particle interaction and flow direction.

621   Table 1. Particle and fluid properties

622   Table 2. Sub-volume dimensions

623   Table 3. Experimental and numerical measurements for each sub-volume

624   Figure S1. Example of the effect of time resolution of PIV analysis on the estimate of the time

625   averaged component (a) u_x and (b) u_y. The velocities are estimated along the yellow dashed

626   lined shown in the inset of (a).

627   Figure S2. Distribution of the number of tracers for a subsets of interrogation windows (32 x 32

628   pixels) for (a) beads and (b) angular particles.

629   Figure S3. Autocorrelation function for a subsets of interrogation windows (32 x 32 pixels) for (a)

630   beads and (b) angular particles. Histogram of autocorrelation peak width for (c) beads and (d)

631   angular particles.

632   V1. Video of an illuminated section in the bead sample showing the movement of tracers

633   V2. Video of an illuminated section in the angular sample showing the movement of tracers

634

Nomenclature

A_{Exp} permeameter cross section area

A_i area of CFD mesh element

d_m characteristic mesh size

d_s seed particle diameter

D diameter of beads and angular particles

D_I interrogation window size

$F_{f \to s}^s$ stokes drag force

$\overline{F}_{f \to s}$ fluid-particle interaction coefficient

$\overline{F}_{f \to s,xz}$ projection of fluid-particle interaction coefficient on x-z plane

$\overline{F}_{f \to s,y}$ projection of fluid-particle interaction coefficient on flow direction – y axis

$\overline{F}_{f \to s}^{ZH}$ fluid-particle interaction coefficient from Zick and Homsy solutions

F_p pressure component of fluid-particle interaction force

F_v viscous component of fluid-particle interaction force

k^{CFD} hydraulic permeability determined through CFD analysis

k^{Exp} hydraulic permeability determined through experimental measurements

k^{PIV} hydraulic permeability determined through PIV analysis

n packing porosity

n_i normal vector of CFD mesh element

N_e number of CFD mesh element on particle surface

p fluid pressure

p_i kinematic normal pressure on CFD mesh element

Q_{Exp} permeameter flow rate

R_{dev} deviatoric stress tensor

Stk_s Stokes number for seed particles

Δt time step used for PIV analysis

u fluid velocity vector

u_x component of fluid velocity in the *x*-direction

u_y component of fluid velocity in the *y*-direction

u_z component of fluid velocity in the *z*-direction

u^s velocity magnitude normalized by mean seepage velocity on each slice

u^v velocity magnitude normalized by mean seepage velocity in each sub-volume

$\langle u^v \rangle$ mean velocity on slice normalized by mean seepage velocity in each sub-volume

u_{seep}^{Exp} seepage velocity determined through experimental measurements

u_{seep}^{PIV} seepage velocity determined through PIV analysis

u_{seep}^{CFD} seepage velocity determined through CFD simulations

v_{seep} seepage flow velocity

μ fluid dynamic viscosity

ρ fluid density

ρ_s seed particle density

v fluid kinematic viscosity

θ_d deviation angle of fluid-particle interaction from the fluid injection direction

635

636   **Acknowledgments**

637

References

Arganda-Carreras, I., Kaynig, V., Rueden, C., Eliceiri, K. W., Schindelin, J., Cardona, A., & Sebastian Seung, H. (2017). Trainable Weka Segmentation: A machine learning tool for microscopy pixel classification. *Bioinformatics*, *33*(15), 2424–2426.

ASTM D 2434-68. (2000). *Standard test method for permeability of granular soils (constant head)*. ASTM International, West Conshohocken, PA.

Atkins, M. (2016). Velocity field measurement using particle image velocimetry (PIV). In *Application of Thermo-Fluidic Measurement Techniques* (pp. 125–166). Elsevier.

Brevis, W., Niño, Y., & Jirka, G. (2011). Integrating cross-correlation and relaxation algorithms for particle tracking velocimetry. *Experiments in Fluids*, *50*(1), 135–147.

Foster, M., Fell, R., & Spannagle, M. (2000). The statistics of embankment dam failures and accidents. *Canadian Geotechnical Journal*, *37*(5), 1000–1024.

Garcia, X., Akanji, L. T., Blunt, M. J., Matthai, S. K., & Latham, J. P. (2009). Numerical study of the effects of particle shape and polydispersity on permeability. *Physical Review E*, *80*(2), 021304. https://doi.org/10.1103/PhysRevE.80.021304

Geuzaine, C., & Remacle, J.-F. (2009). Gmsh: A 3-D finite element mesh generator with built-in pre-and post-processing facilities. *International Journal for Numerical Methods in Engineering*, *79*(11), 1309–1331.

Gollin, D., Brevis, W., Bowman, E. T., & Shepley, P. (2017). Performance of PIV and PTV for granular flow measurements. *Granular Matter*, *19*(3), 42.

Huang, A. Y., Huang, M. Y., Capart, H., & Chen, R.-H. (2008). Optical measurements of pore geometry and fluid velocity in a bed of irregularly packed spheres. *Experiments in Fluids*, *45*(2), 309–321.

Hunter, R. P., & Bowman, E. T. (2018). Visualisation of seepage-induced suffusion and suffosion within internally erodible granular media. *Géotechnique*, *68*(10), 918–930. https://doi.org/10.1680/jgeot.17.P.161

ICOLD, C. (2015). Internal erosion of existing dams, levees and dikes, and their foundations. *Bulletin*.

Iskander, M., Bathurst, R., & Omidvar, M. (2015). Past, present, and future of transparent soils. *Geotechnical Testing Journal*, *38*(5), 557–573.

Karadimitriou, N., & Hassanizadeh, S. (2012). A review of micromodels and their use in two-phase flow studies. *Vadose Zone Journal*, *11*(3), vzj2011-0072.

Karadimitriou, N., Musterd, M., Kleingeld, P., Kreutzer, M., Hassanizadeh, S., & Joekar-Niasar, V. (2013). On the fabrication of PDMS micromodels by rapid prototyping, and their use in two-phase flow studies. *Water Resources Research*, *49*(4), 2056–2067.

Keane, R. D., & Adrian, R. J. (1993). Theory and simulation of particle image velocimetry. *Fifth International Conference on Laser Anemometry: Advances and Applications*, *2052*, 477–492.

676   Khalili, A., Basu, A., & Pietrzyk, U. (1998). Flow visualization in porous media via positron
677   emission tomography. *Physics of Fluids*, *10*(4), 1031–1033.
678   Knight, C., O'Sullivan, C., van Wachem, B., & Dini, D. (2020). Computing drag and interactions
679   between fluid and polydisperse particles in saturated granular materials. *Computers and*
680   *Geotechnics*, *117*, 103210. https://doi.org/10.1016/j.compgeo.2019.103210
681   Lorensen, W. E., & Cline, H. E. (1987). Marching cubes: A high resolution 3D surface
682   construction algorithm. *ACM Siggraph Computer Graphics*, *21*(4), 163–169.
683   Meinhart, C. D., Wereley, S. T., & Santiago, J. G. (1999). PIV measurements of a microchannel
684   flow. *Experiments in Fluids*, *27*(5), 414–419.
685   Michaelis, D., Neal, D. R., & Wieneke, B. (2016). Peak-locking reduction for particle image
686   velocimetry. *Measurement Science and Technology*, *27*(10), 104005.
687   Mostaghimi, P., Blunt, M. J., & Bijeljic, B. (2013). Computations of absolute permeability on
688   micro-CT images. *Mathematical Geosciences*, *45*(1), 103–125.
689   Muir Wood, D. (2007). The magic of sands—The 20th Bjerrum Lecture presented in Oslo, 25
690   November 2005. *Canadian Geotechnical Journal*, *44*(11), 1329–1350.
691   Northrup, M. A., Kulp, T. J., Angel, S. M., & Pinder, G. F. (1993). Direct measurement of
692   interstitial velocity field variations in a porous medium using fluorescent-particle image
693   velocimetry. *Chemical Engineering Science*, *48*(1), 13–21.
694   Nunes, J. P., Bijeljic, B., & Blunt, M. (2015). Time-of-flight distributions and breakthrough
695   curves in heterogeneous porous media using a pore-scale streamline tracing algorithm.
696   *Transport in Porous Media*, *109*(2), 317–336.
697   OpenFOAM Foundation. (2019). *OpenFOAM v7 User Guide*. https://cfd.direct/openfoam/user-
698   guide
699   Otsu, N. (1979). A threshold selection method from gray-level histograms. *IEEE Transactions*
700   *on Systems, Man, and Cybernetics*, *9*(1), 62–66.
701   Patil, V. A., & Liburdy, J. A. (2013). Flow characterization using PIV measurements in a low
702   aspect ratio randomly packed porous bed. *Experiments in Fluids*, *54*(4), 1497.
703   Peurrung, L. M., Rashidi, M., & Kulp, T. J. (1995). Measurement of porous medium velocity
704   fields and their volumetric averaging characteristics using particle tracking velocimetry.
705   *Chemical Engineering Science*, *50*(14), 2243–2253.
706   Piller, M., Casagrande, D., Schena, G., & Santini, M. (2014). Pore-scale simulation of laminar
707   flow through porous media. *Journal of Physics: Conference Series*, *501*(1), 012010.
708   Preene, M., & Rosser, M. (2012). *Groundwater lowering in construction: A practical guide to*
709   *dewatering* (Vol. 6). CRC Press.
710   Rong, L. W., Dong, K. J., & Yu, A. B. (2013). Lattice-Boltzmann simulation of fluid flow
711   through packed beds of uniform spheres: Effect of porosity. *Chemical Engineering*
712   *Science*, *99*, 44–58. https://doi.org/10.1016/j.ces.2013.05.036

713 Ronneberger, O., Fischer, P., & Brox, T. (2015). U-net: Convolutional networks for biomedical
714   image segmentation. *International Conference on Medical Image Computing and*
715   *Computer-Assisted Intervention*, 234–241.
716 Saleh, S., Thovert, J., & Adler, P. (1992). Measurement of two-dimensional velocity fields in
717   porous media by particle image displacement velocimetry. *Experiments in Fluids*, *12*(3),
718   210–212.
719 Sanvitale, N., & Bowman, E. T. (2012). Internal imaging of saturated granular free-surface
720   flows. *International Journal of Physical Modelling in Geotechnics*, *12*(4), 129–142.
721 Schindelin, J., Arganda-Carreras, I., Frise, E., Kaynig, V., Longair, M., Pietzsch, T., Preibisch,
722   S., Rueden, C., Saalfeld, S., Schmid, B., & others. (2012). Fiji: An open-source platform
723   for biological-image analysis. *Nature Methods*, *9*(7), 676–682.
724 Sederman, A., Johns, M., Bramley, A., Alexander, P., & Gladden, L. (1997). Magnetic resonance
725   imaging of liquid flow and pore structure within packed beds. *Chemical Engineering*
726   *Science*, *52*(14), 2239–2250.
727 Soille, P. (2013). *Morphological image analysis: Principles and applications*. Springer Science
728   & Business Media.
729 Taylor, H., O'sullivan, C., & Sim, W. (2016). Geometric and hydraulic void constrictions in
730   granular media. *Journal of Geotechnical and Geoenvironmental Engineering*, *142*(11),
731   04016057.
732 Taylor, H., O'Sullivan, C., Sim, W. W., & Carr, S. J. (2017). Sub-particle-scale investigation of
733   seepage in sands. *Soils and Foundations*, *57*(3), 439–452.
734 Thaker, A. H., Karthik, G., & Buwa, V. V. (2019). PIV measurements and CFD simulations of
735   the particle-scale flow distribution in a packed bed. *Chemical Engineering Journal*, *374*,
736   189–200.
737 Thielicke, W. (2014). *The flapping flight of birds: Analysis and application* [PhD Thesis].
738   University of Groningen.
739 Thielicke, W., & Stamhuis, E. (2014). PIVlab–towards user-friendly, affordable and accurate
740   digital particle image velocimetry in MATLAB. *Journal of Open Research Software*,
741   *2*(1).
742 Vogt, N., Simpson, B., Van Seters, A., Gens, A., Odenwald, B., Moller, H., Habert, J., & Panu,
743   T. (2015). TC250/SC7/EG9: Water pressures. *Final Report: Proposal of Changes to*
744   *EC7-1*.
745 Wiederseiner, S., Andreini, N., Epely-Chauvin, G., & Ancey, C. (2011). Refractive-index and
746   density matching in concentrated particle suspensions: A review. *Experiments in Fluids*,
747   *50*(5), 1183–1206.
748 Zhang, L., & Chen, Q. (2006). Seepage failure mechanism of the Gouhou rockfill dam during
749   reservoir water infiltration. *Soils and Foundations*, *46*(5), 557–568.
750 Zhao, B., Wang, J., Coop, M., Viggiani, G., & Jiang, M. (2015). An investigation of single sand
751   particle fracture using X-ray micro-tomography. *Géotechnique*, *65*(8), 625–641.

752   Zick, A. A., & Homsy, G. M. (1982). Stokes flow through periodic arrays of spheres. *Journal of*

753   *Fluid Mechanics*, *115*(1), 13. https://doi.org/10.1017/S0022112082000627

754

755

756   Table 1. Particle and fluid properties

	Particle diameter [mm]	Density [g/cm^3]	Refractive index	Viscosity	
				Kinematic [mm^2/s]	Dynamic [Pa·s]
SiLibeads Glass beads Type P Borosilicate	7.5 ± 0.03	2.23	1.46 (*)	-	
Duran® angular particles	6.7 – 9.5	2.23	1.47 (at 21°C)	-	
Cargille immersion fluid	-	0.846	1.47 (at 25°C)	16 (at 25 ℃)	0.0135
Microsphere fluid seeding particles	0.005 – 0.030	0.750	-	-	

757   (*) The measurement temperature for the refractive index value was not given on the material certificate.
758   A sensitivity analysis to temperature was conducted to achieve the optimum optical transparency with the
759   immersion fluid.

760

761

762

763   Table 2. Sub-volume dimensions

Sub-volume	Dimensions, x × y × z [mm^3]
Beads-U	37.4 × 23.4 × 25
Beads-L	40.4 × 25.3 × 25
Ang-U	38.5 × 24.0 × 25
Ang-L	38.5 × 24.0 × 25

764

765

766

767

768

769   Table 3. Experimental and numerical measurements for each sub-volume

Sub-volume	n	i_{Exp}	A_{Exp} [cm^2]	Q_{Exp} [ml/s]	u_{seep}^{Exp} [mm/s]	u_{seep}^{PIV} [mm/s]	u_{seep}^{CFD} [mm/s]
Beads-U	0.38	0.086	100	30.3	8.0	7.1	6.8
Beads-L	0.38	0.086	100	30.3	8.0	5.7	6.2
Ang-U	0.36	0.143	100	28.5	7.9	4.5	6.0
Ang-L	0.36	0.114	100	28.5	7.9	4.5	5.9

770

Figure 1. Schematic of the experimental set up.
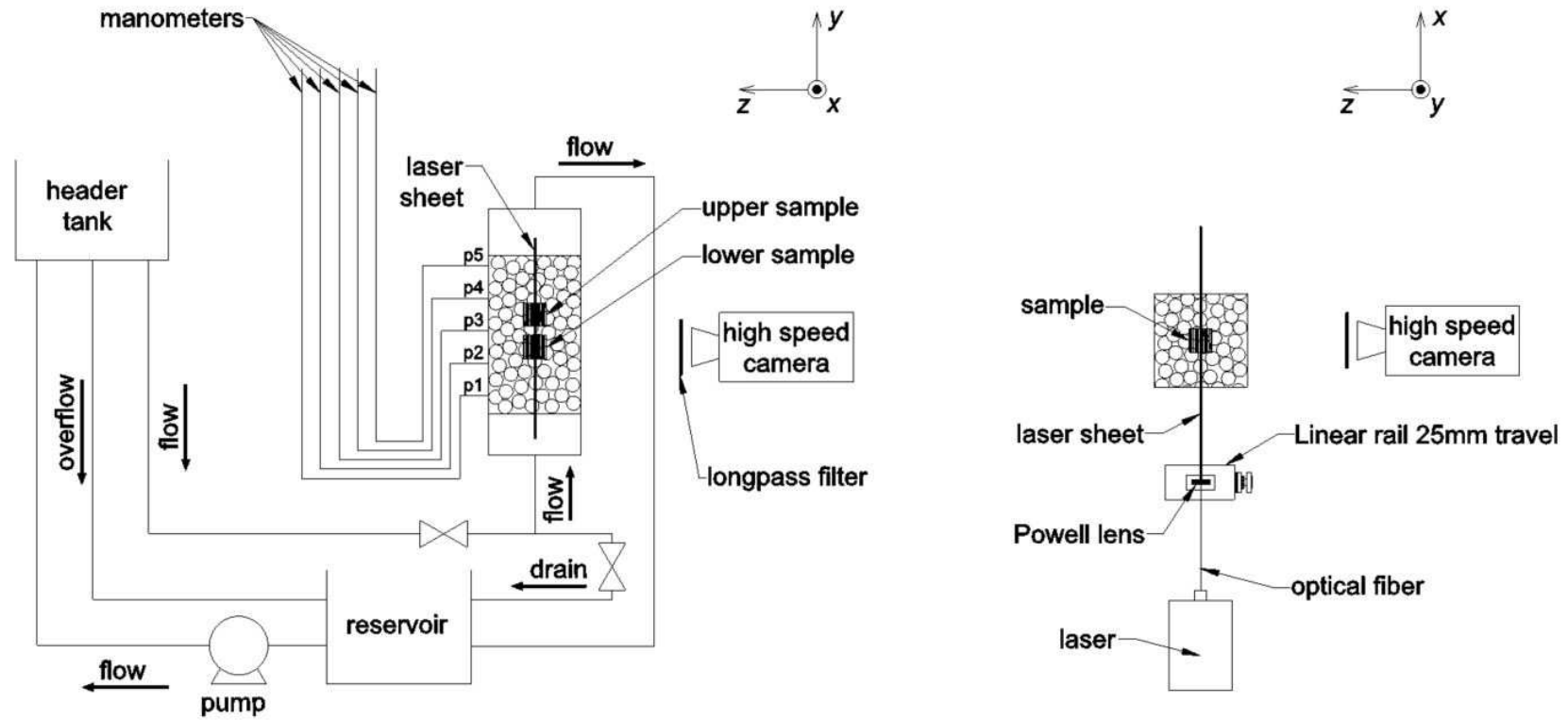
Figure 2. Images of experimental setup: (a) Permeameter cell partially filled with oil; (b) Beads sample illuminated by laser sheet; (c) Angular particles sample illuminated by laser sheet; (d) top view of the laser sheet.
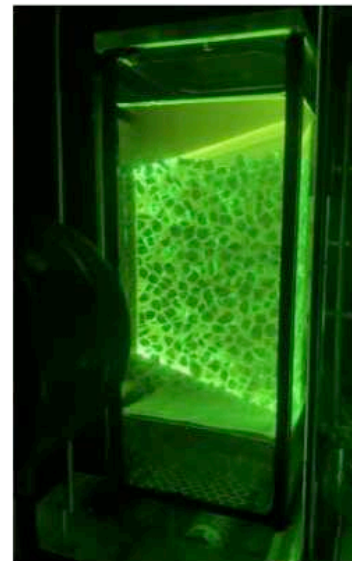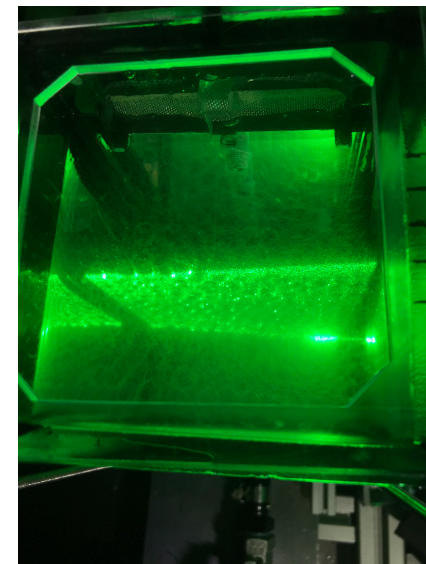
Figure 3. Flow fields in the (a) left, (b) middle and (c) right for the permeameter with beads.
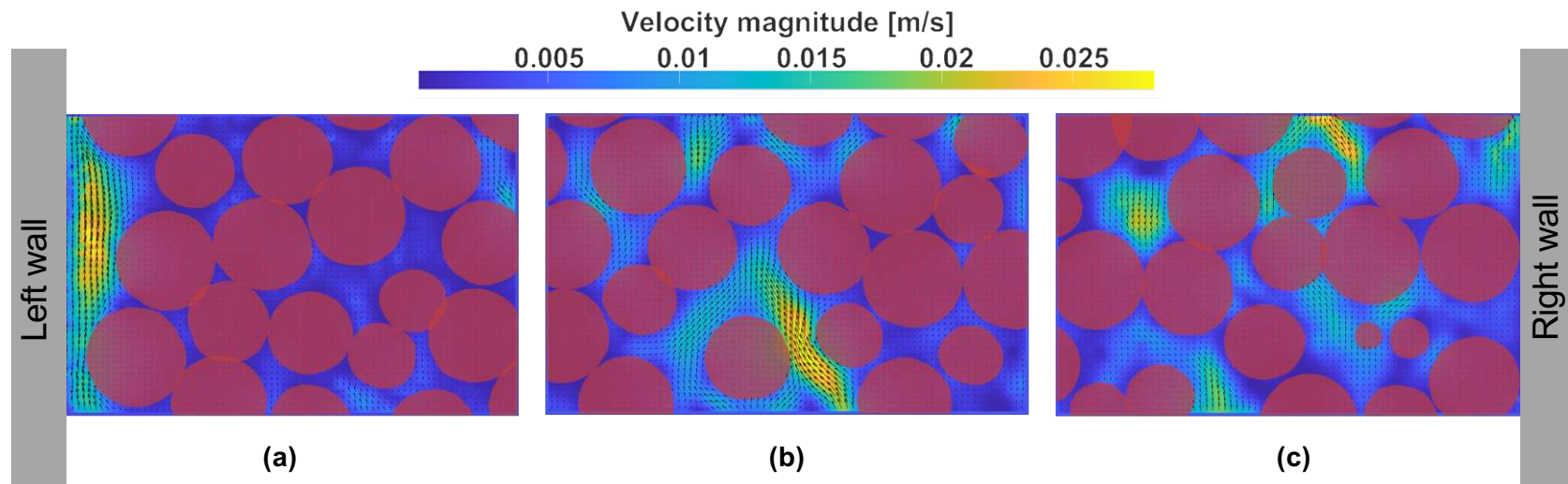
Figure 4. (a) Typical grey-scale image in Beads-U sub-volume, $z = 0$ mm. (b) Histogram of grey values. Inset in (a) shows that the non-uniform intensity is a consequence of the finite laser width.
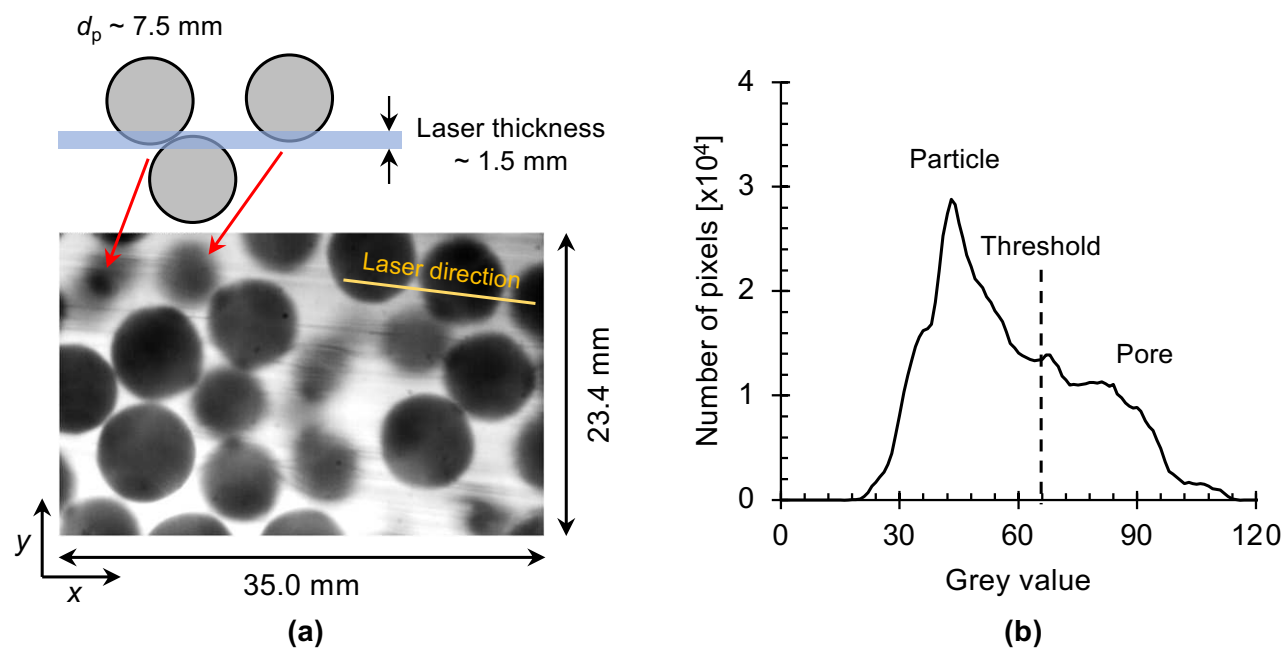
(a)

(b)

Figure 5. Segmentation results for three typical slices in Beads-U sub-volume using three different segmentation methods: threshold segmentation with Otsu's threshold, trainable Weka segmentation, and U-Net segmentation. Note: dashed circles indicate the artifacts produced by inaccurate segmentation.
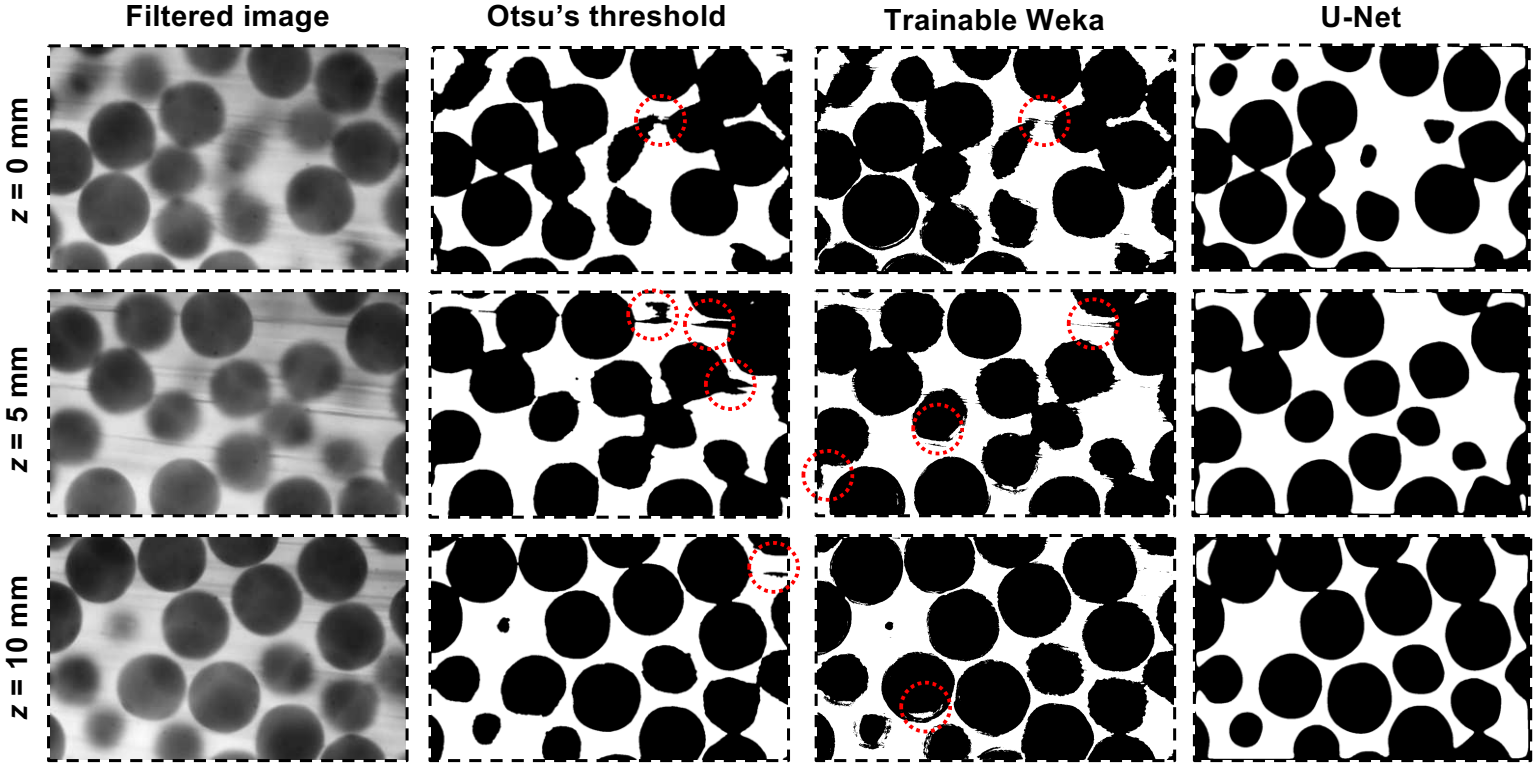
Figure 6. U-Net segmentation procedure for Beads-U sub-volume: (a) Step-1: prepare training and validating data sets; (b) Step-2: train U-Net algorithm; (c) Step-3: apply trained U-Net as a classifier for segmenting new images.
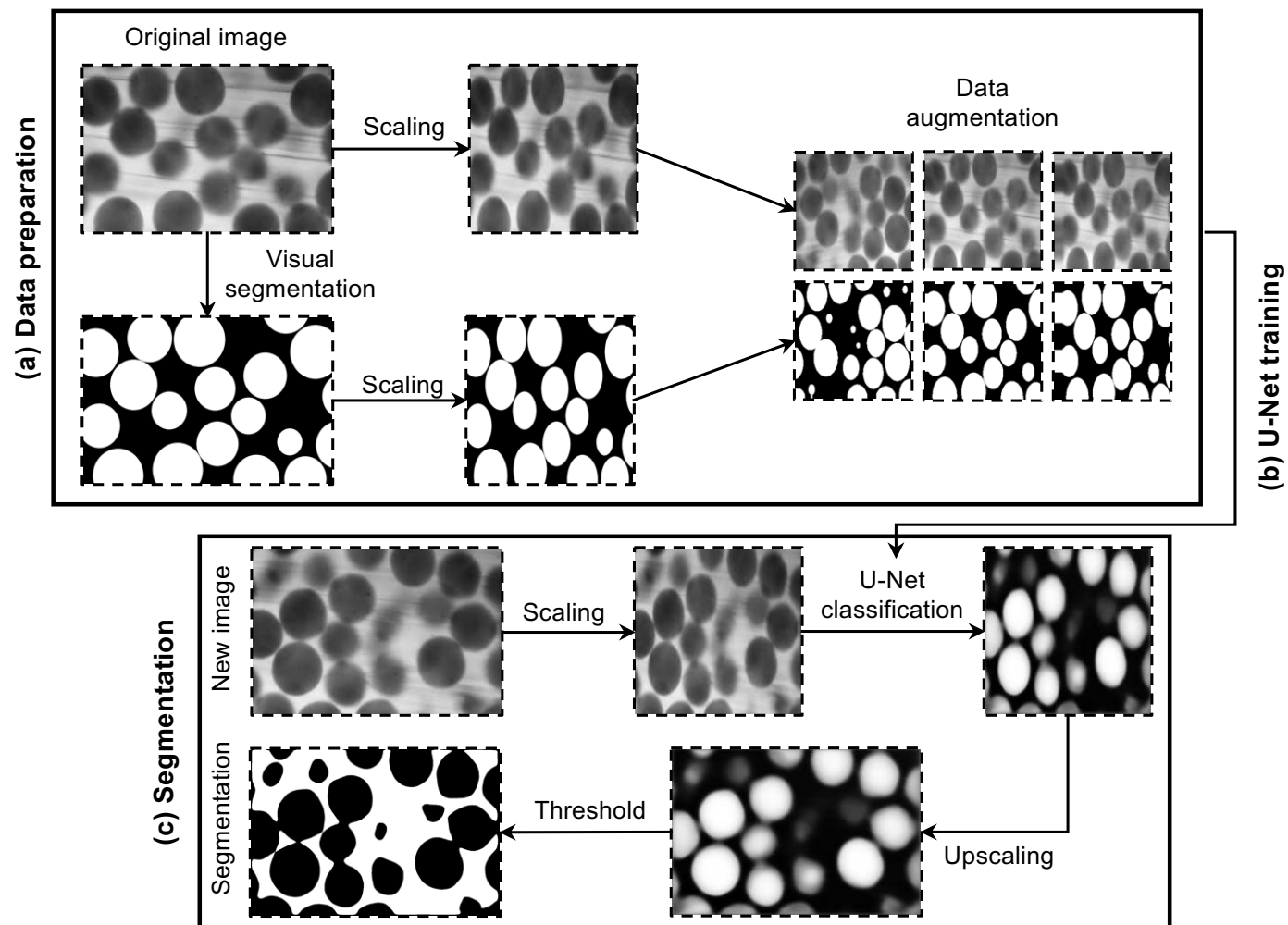
Figure 7. Upscaling along *z*-direction on the U-Net classified image for Beads-U sub-volume: (a) Unscaled image data; (b) Image obtained by scaling without interpolation; (c) Image obtained by scaling with bilinear interpolation; (d) Image obtained by scaling with bicubic interpolation.
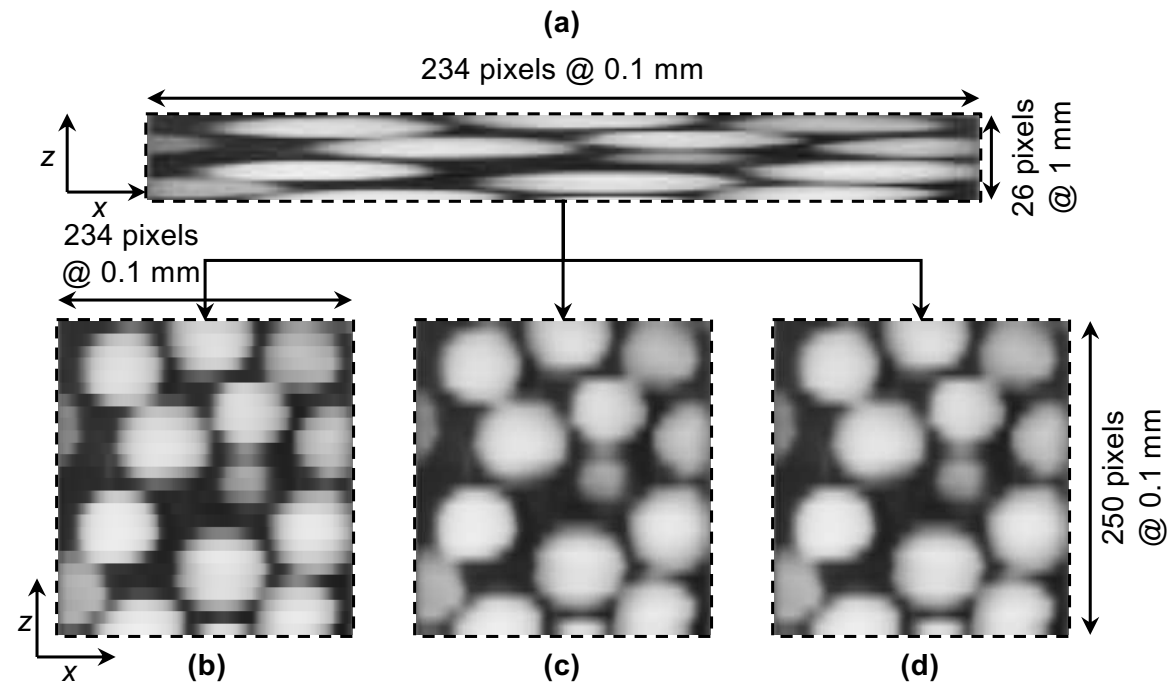
Figure 8. Labelled images with particles represented by different colours for Beads-U sub-volume on (a) x-y plane and (b) x-z plane and Ang-U sub-volume on (c) x-y plane and (d) x-z plane.
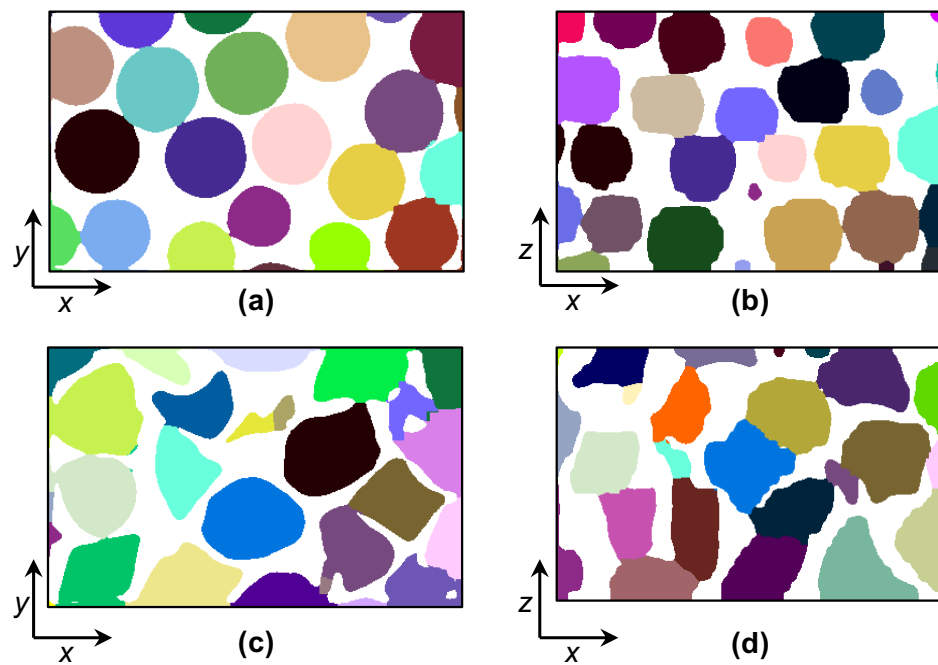
Figure 9. Three-dimensional views of the combined surface meshes for (a) Beads-U sub-volume and (b) Ang-U sub-volume. Note: colour is used to distinguish the surfaces of individual particles. Hexahedron meshes which discretize pore structure for CFD simulation for (c) Beads-U sub-volume and (d) Ang-U sub-volume.
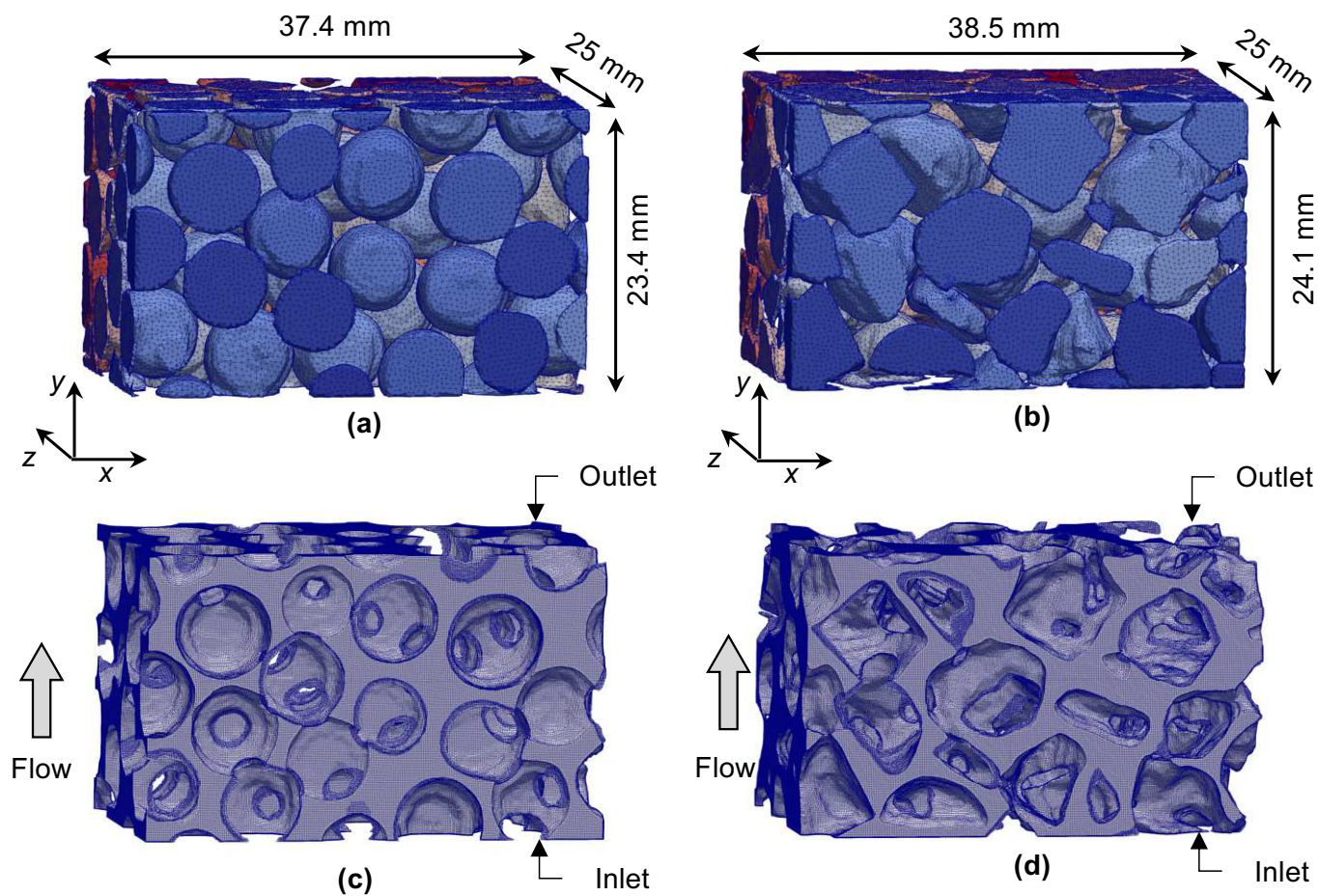
Figure 10. Verification of CFD modelling approach: (a) Confirmation of ability to capture the influence of porosity on the fluid-particle interaction coefficient $\bar{F}_{f \to s}$, dashed lines indicate a curve fit to the Zick & Homsy (1982) data; (b) Mesh dependence of $\bar{F}_{f \to s}$ for SC packings; (c) Mesh dependence of $\bar{F}_{f \to s}$ for FCC packings. The results predicted by the Immersed Boundary Method (IBM) with a regular grid and from fully resolved CFD using an unstructured meshes from Knight et al. (2020) are included in (a) and (c), respectively.
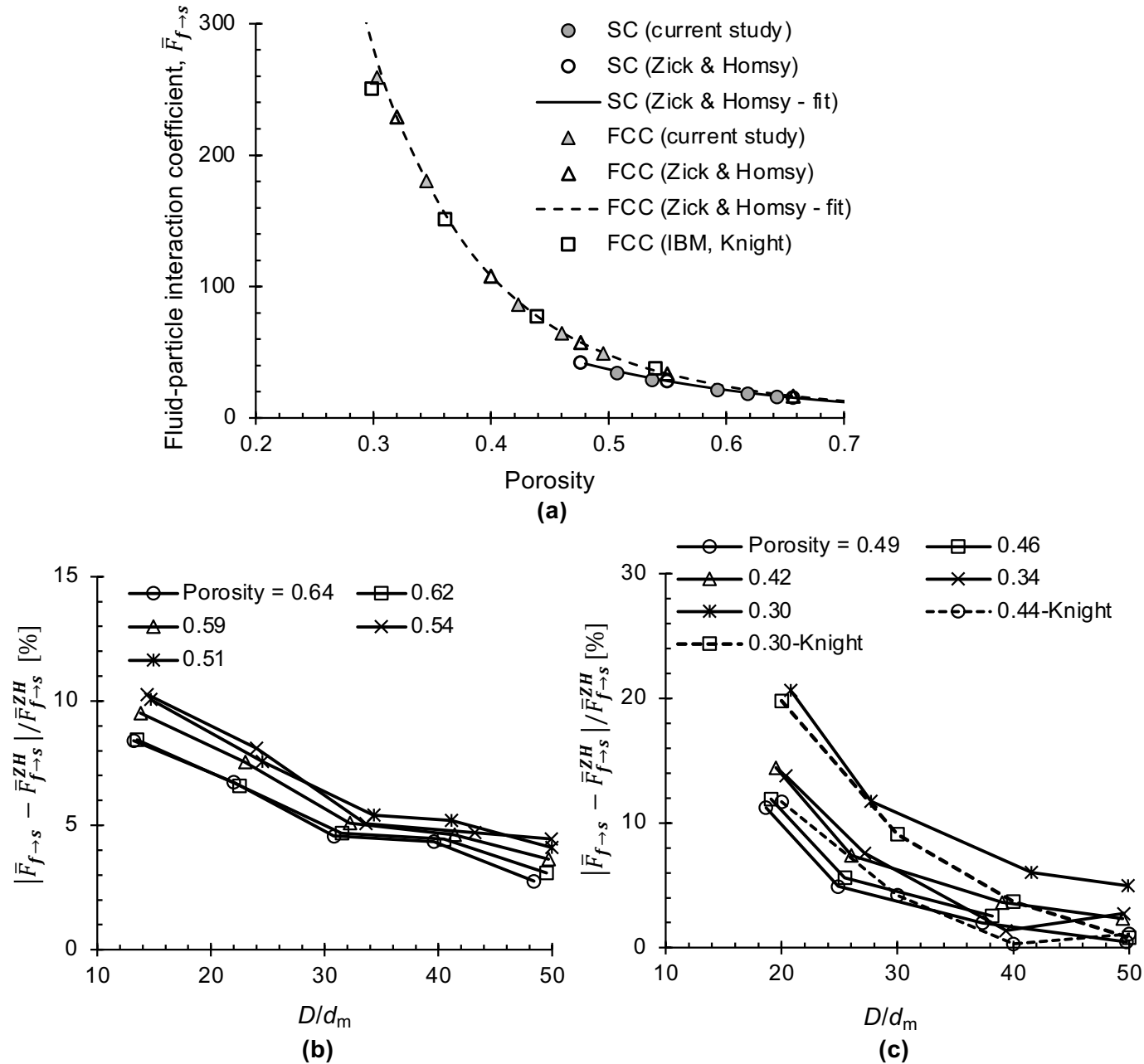
Figure 11. (a) Hydraulic permeability values predicted by experiments, PIV and CFD measurements. (b) Influence of porosity on hydraulic permeability as estimated by CFD modelling for Beads-U and Ang-U sub-volumes. The prediction results from Kozeny-Carman Equation (KC Eq.) is included in (b).
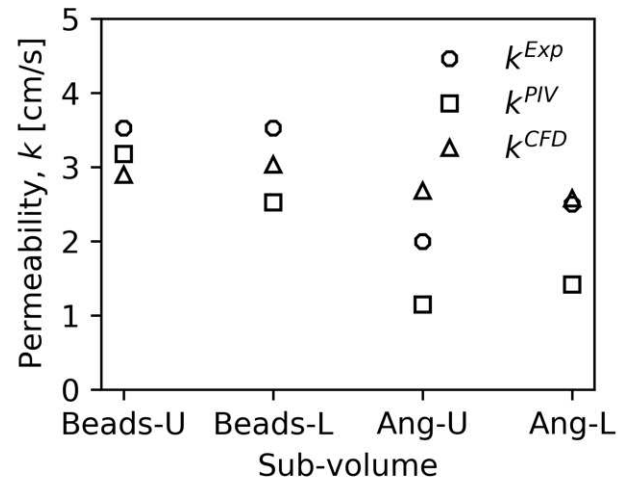
(a)
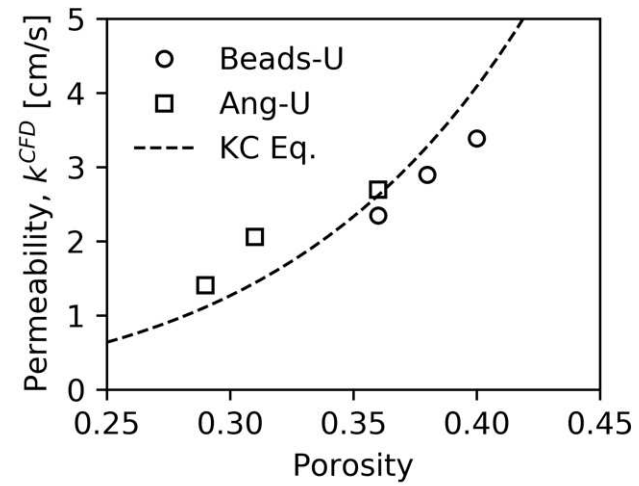
(b)

Figure 12. Comparison of the PIV and CFD flow fields in Beads-U sub-volume on the vertical slice with z = 16 mm.
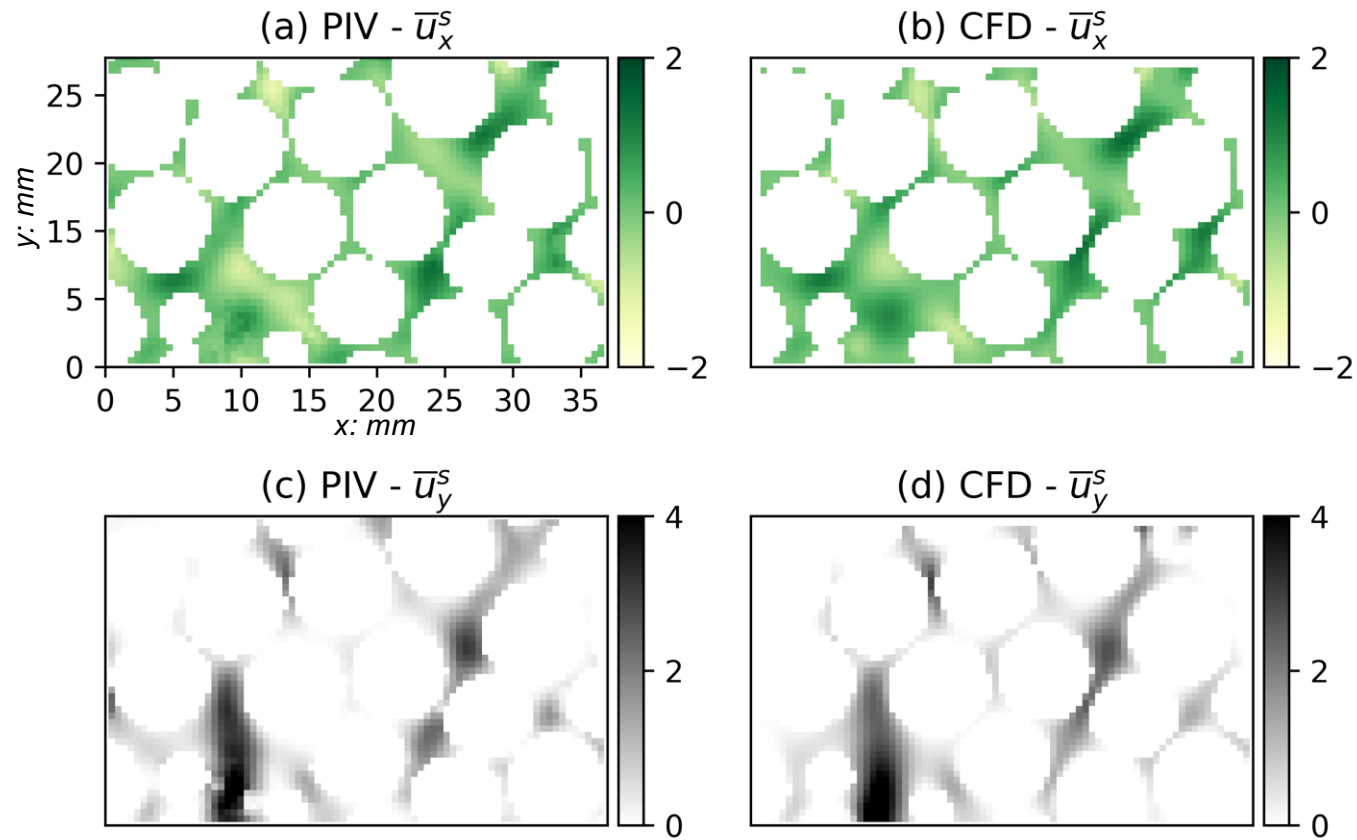
Figure 13. Comparison of the PIV and CFD flow fields in Beads-U sub-volume on three slices with z= 1, 8 and 16 mm. Velocity vector length is normalized by seepage velocity.

$$\overline{u}^{s}_{xy} = 4$$
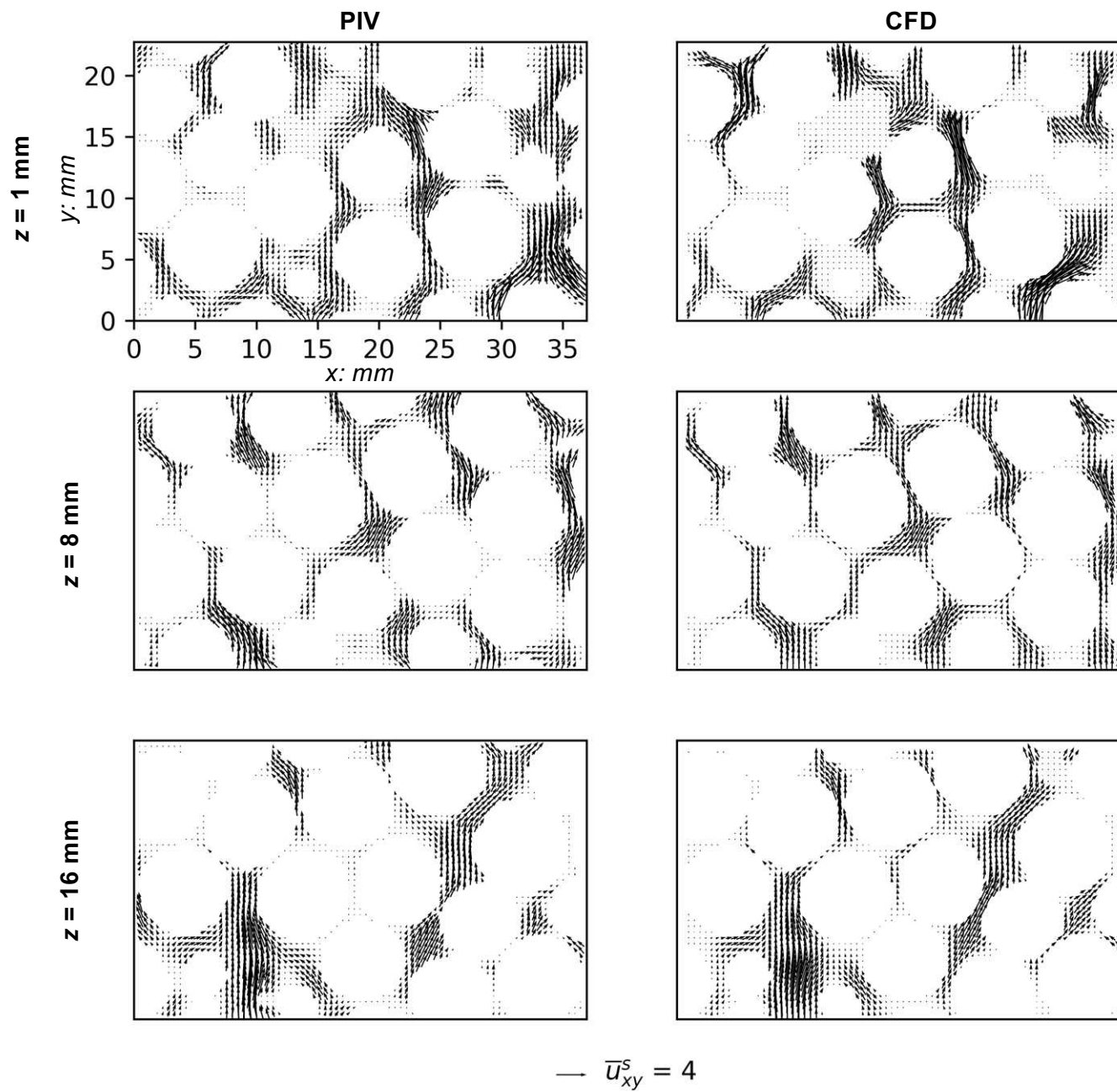
Figure 14. Cumulative distributions of flow velocity at four vertical planes in Beads-U sub-volume obtained from PIV and CFD results.
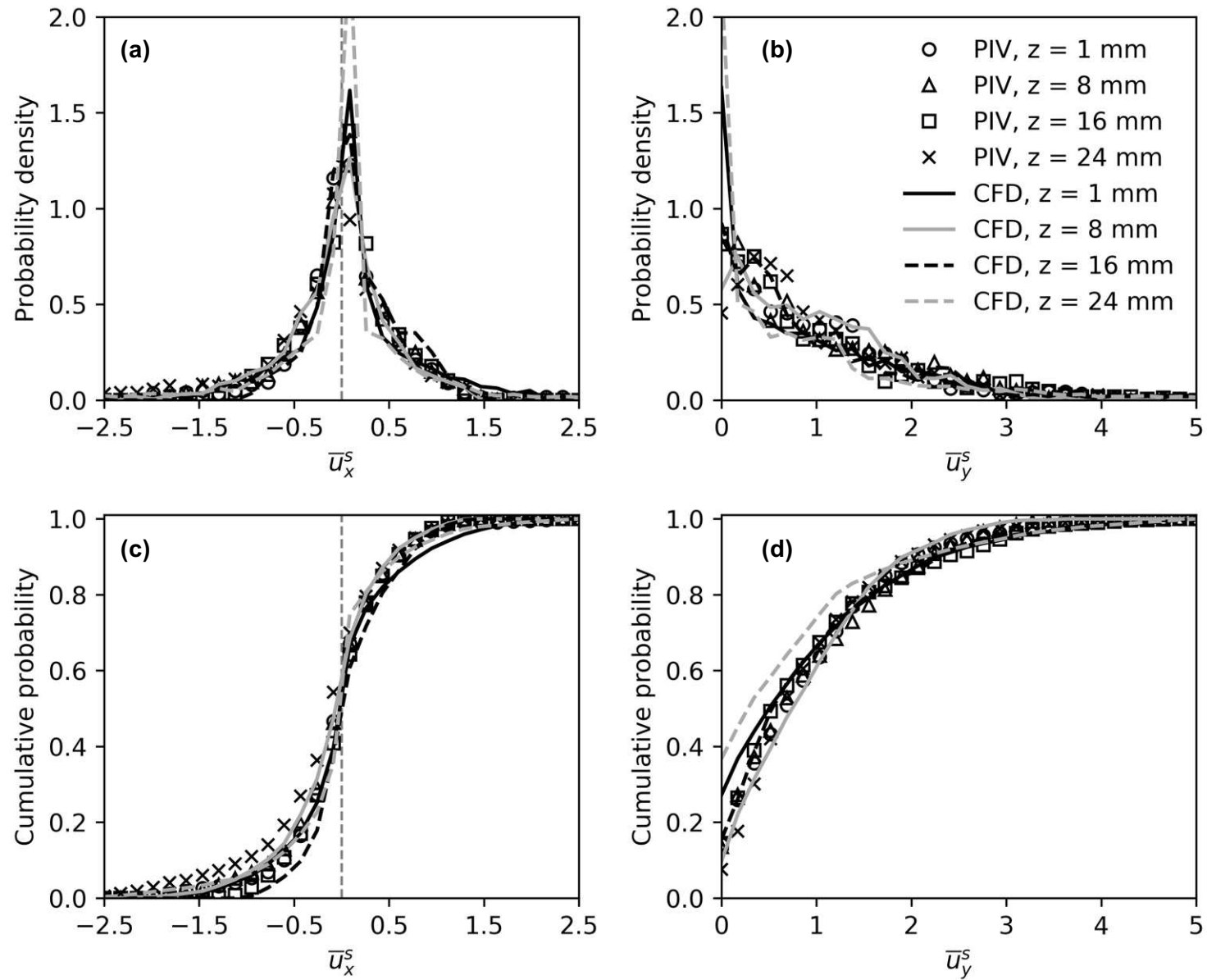
Figure 15. Comparison of the PIV and CFD flow fields in Ang-L sub-volume on three slices with z = 1, 8 and 16 mm. Velocity vector length is normalized by seepage velocity. Arrows indicate narrow flow paths.
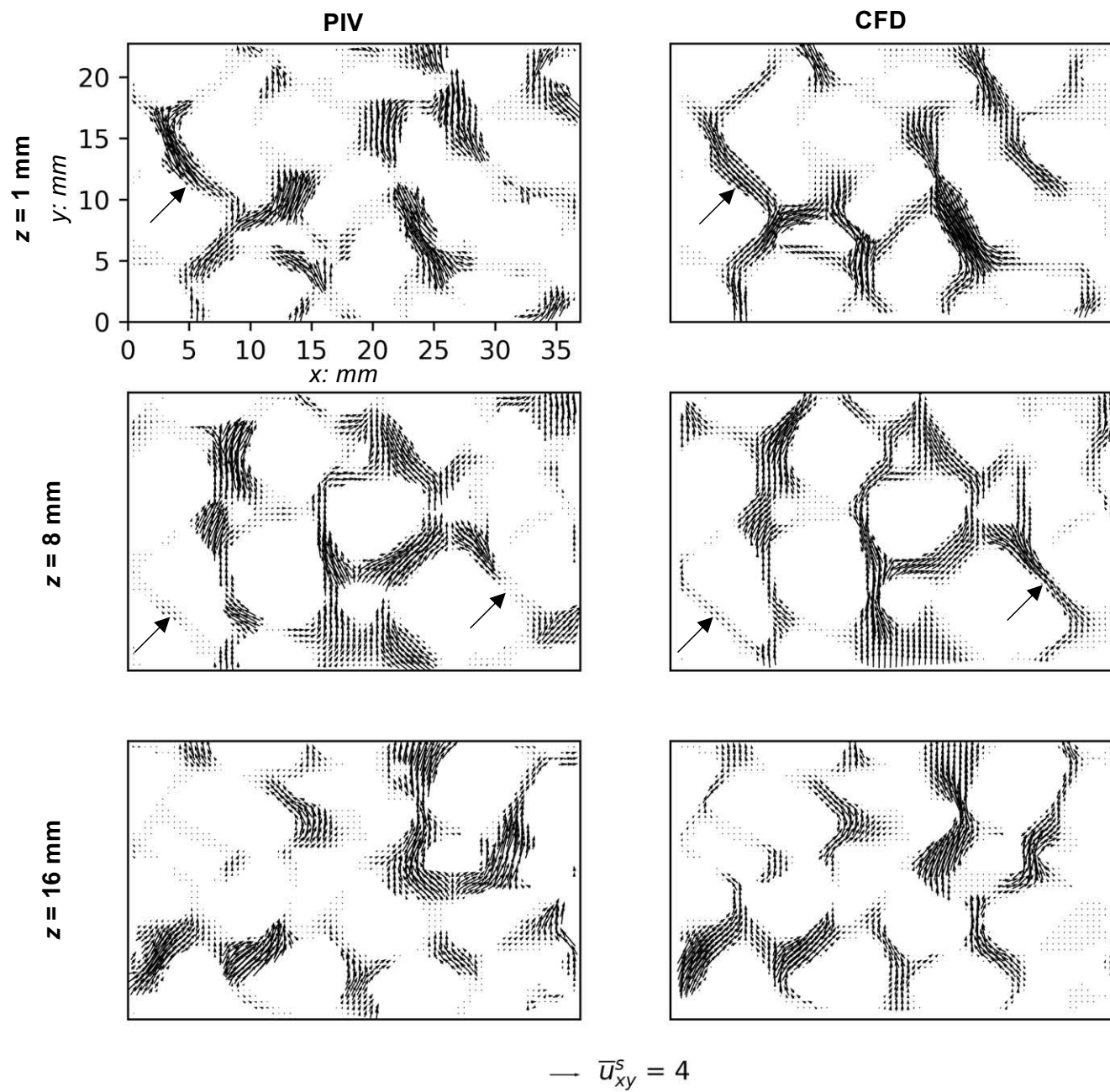
Figure 16. Cumulative distributions of flow velocity at four vertical planes in Ang-L sub-volume obtained from PIV and CFD results.
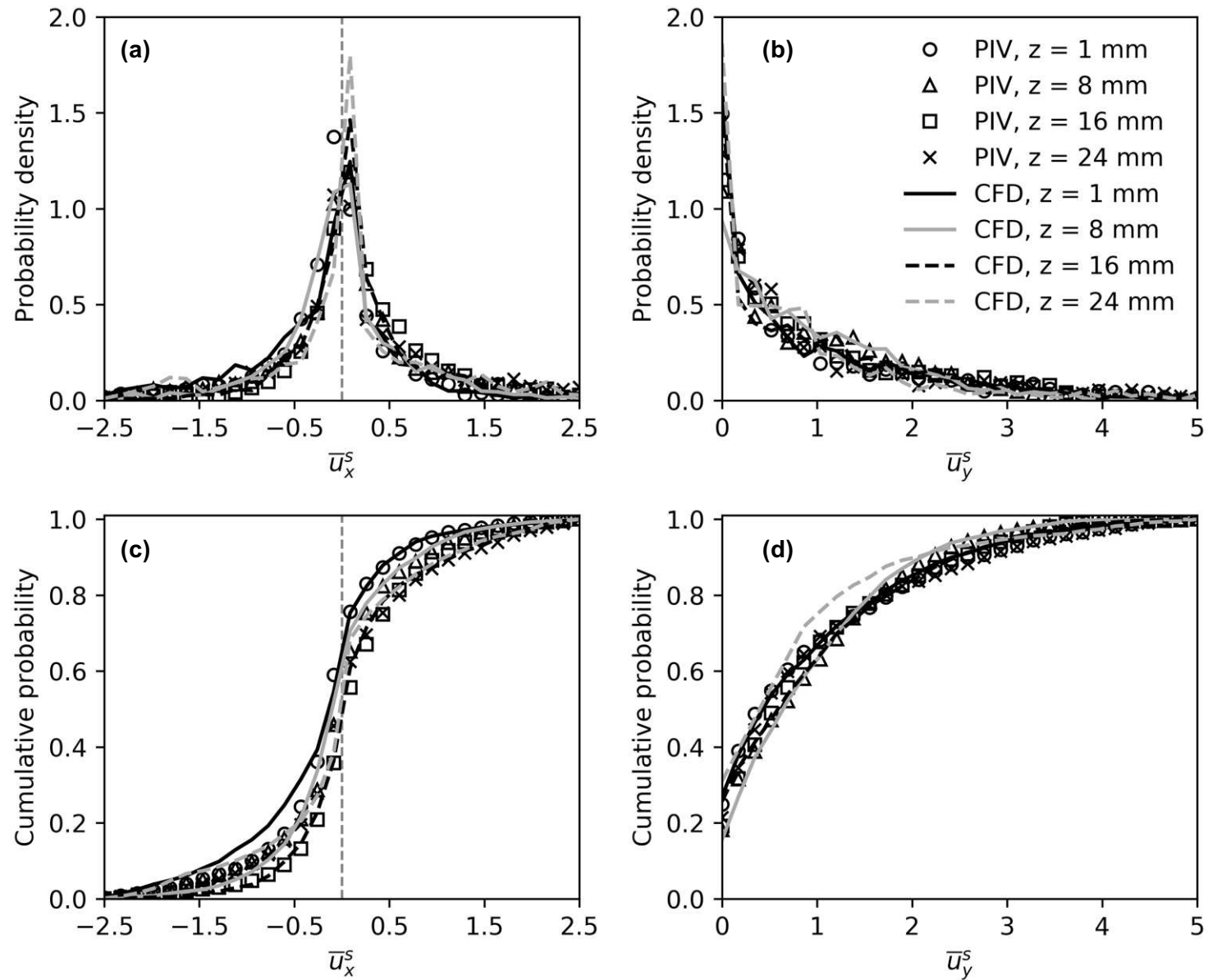
Figure 17. Difference between PIV and CFD flow fields for the vertical slice with $z = 16$ mm in Beads-U sub-volume: (a) horizontal velocity; (b) vertical velocity. The cumulative distributions of PIV and CFD difference for (c) horizontal velocity and (d) vertical velocity on five typical slices in Beads-U sub-volume.
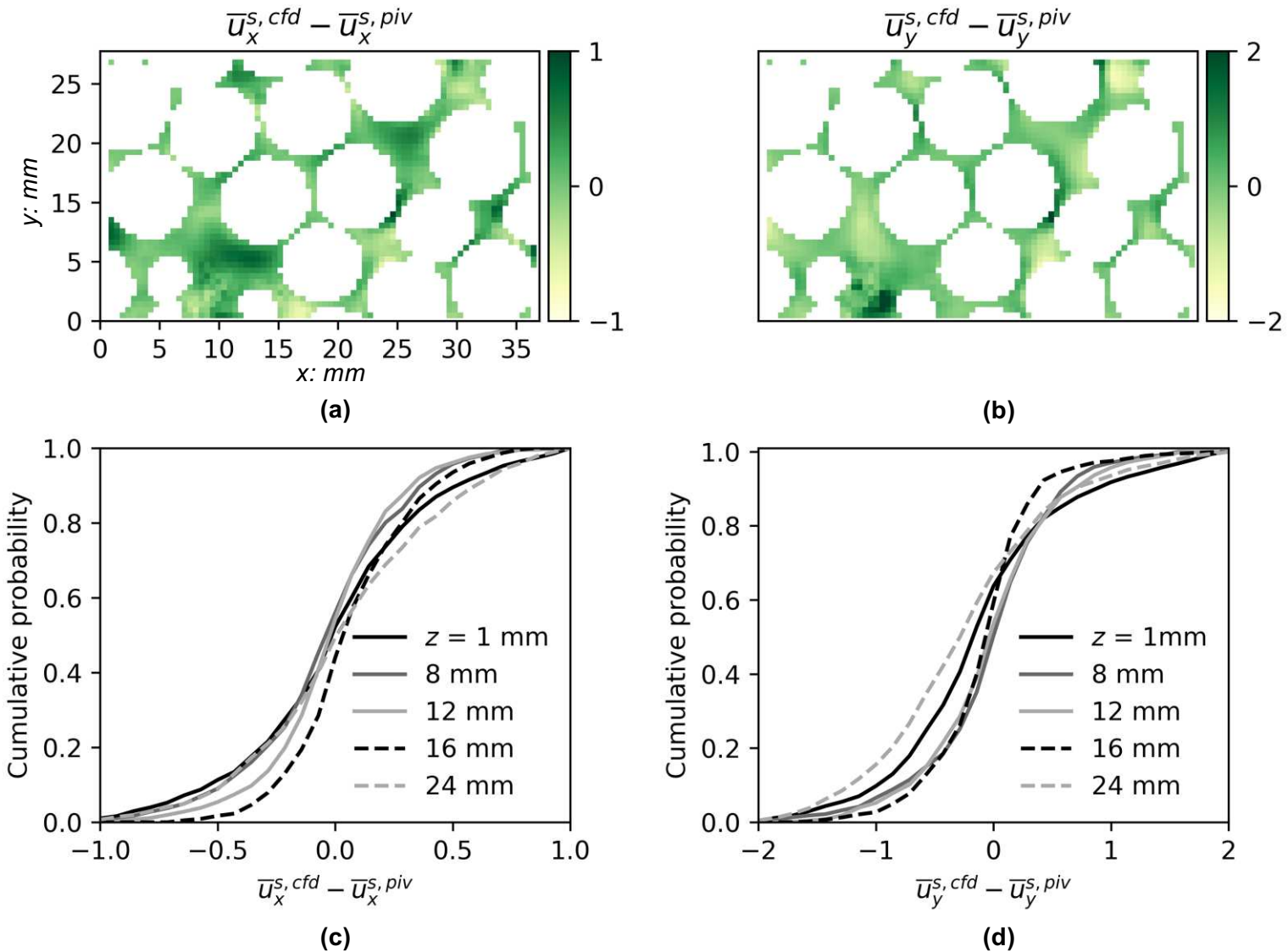
Figure 18. Variation of the mean velocity values obtained from PIV and CFD results and the slice porosity on x-y planes parallel to flow direction.
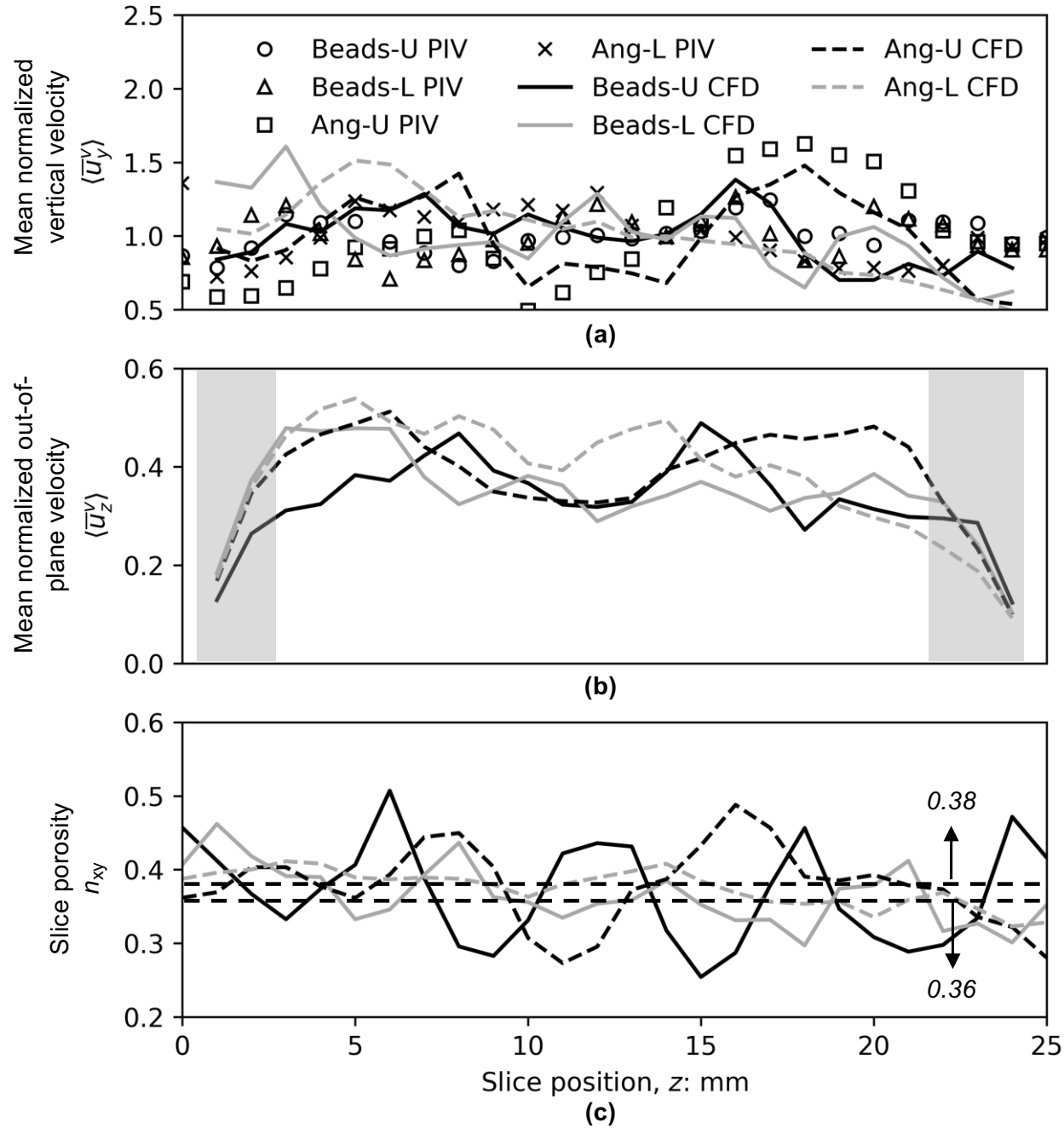
Figure 19. Variation of mean vertical velocity, porosity and hydraulic gradient on x-z planes perpendicular to flow direction predicted by CFD simulations.
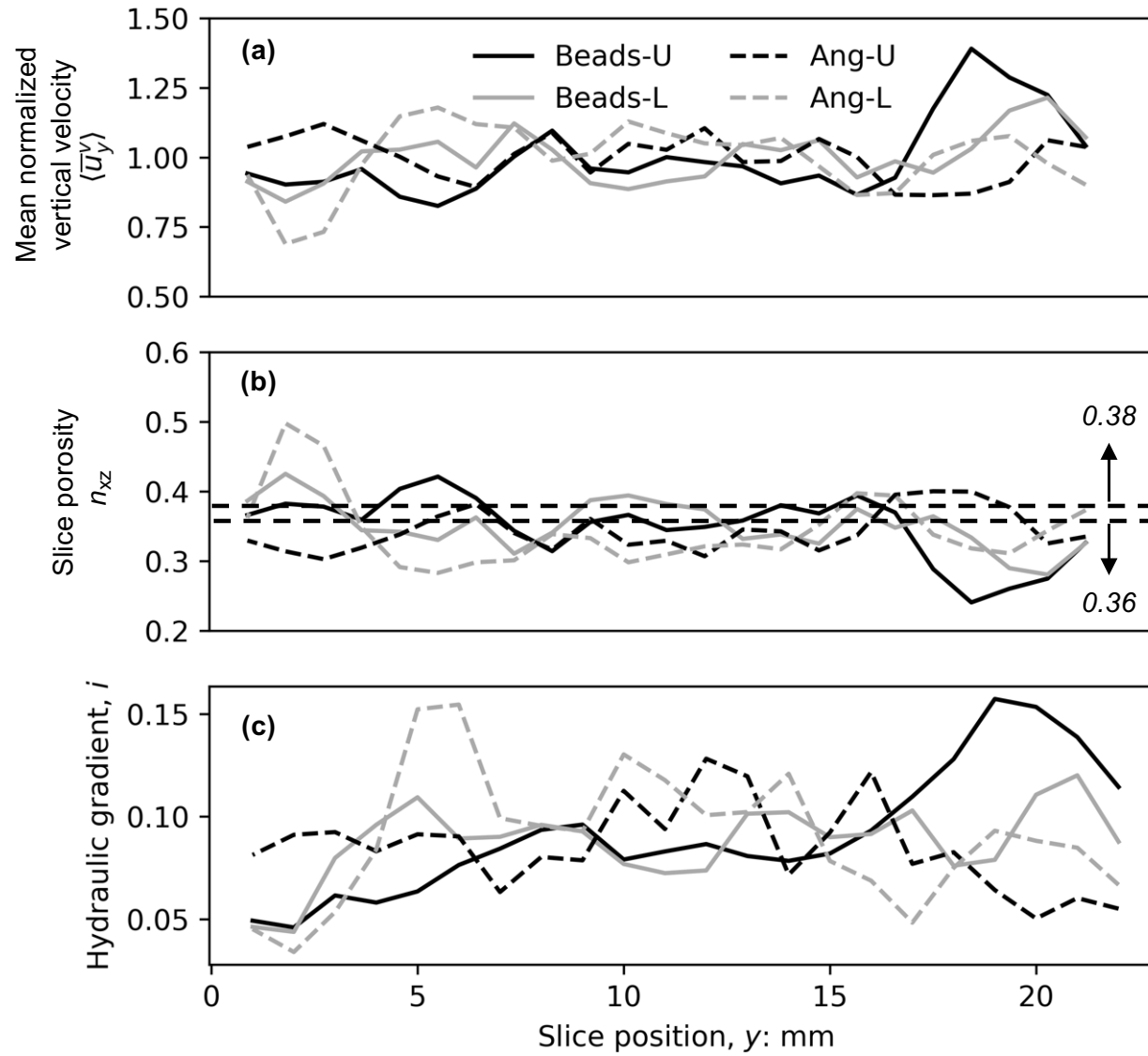
Figure 20. Projection views of drag force vectors for the particles that are not intersecting with boundary walls.
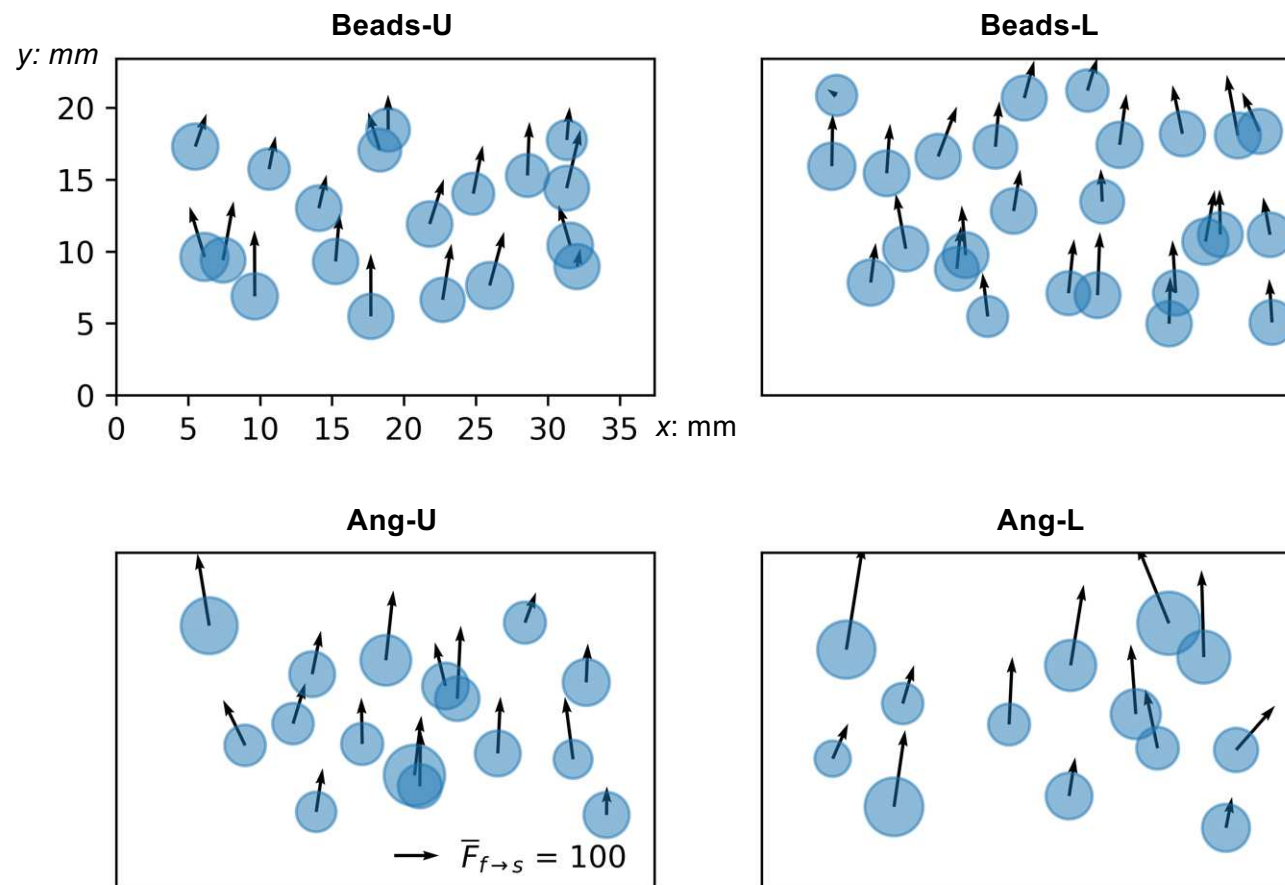
Figure 21. Cumulative distributions of (a) fluid-particle interaction coefficients for beads and angular particles and (b) the normalized fluid-particle interaction coefficients.
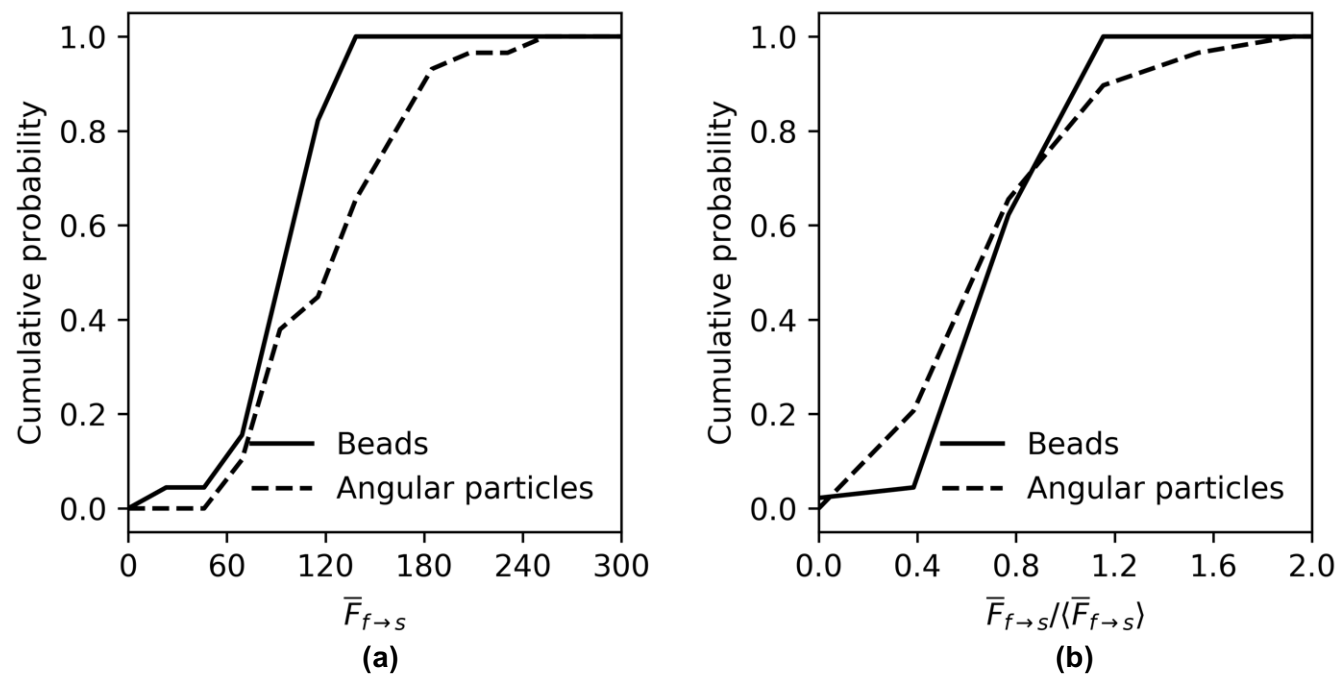
Figure 22. Distributions of (a) the ratio between pressure and viscous drag components, and (b) the angle between fluid-particle interaction and flow direction.
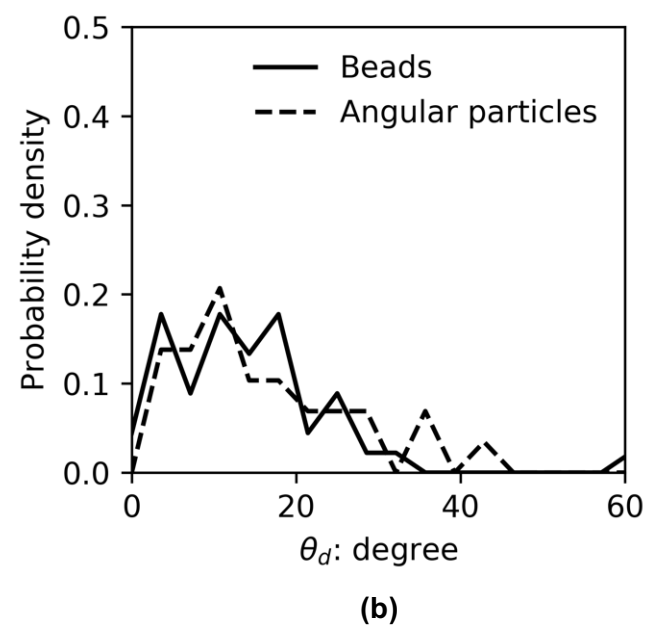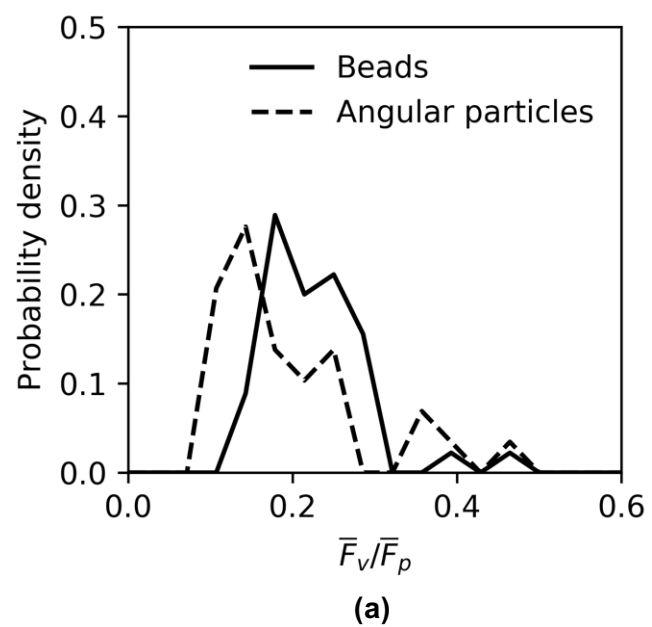
(a)

(b)

Figure S1. Example of the effect of time resolution of PIV analysis on the estimate of the time averaged component (a) u_x and (b) u_y. The velocities are estimated along the yellow dashed lined shown in the inset of (a).
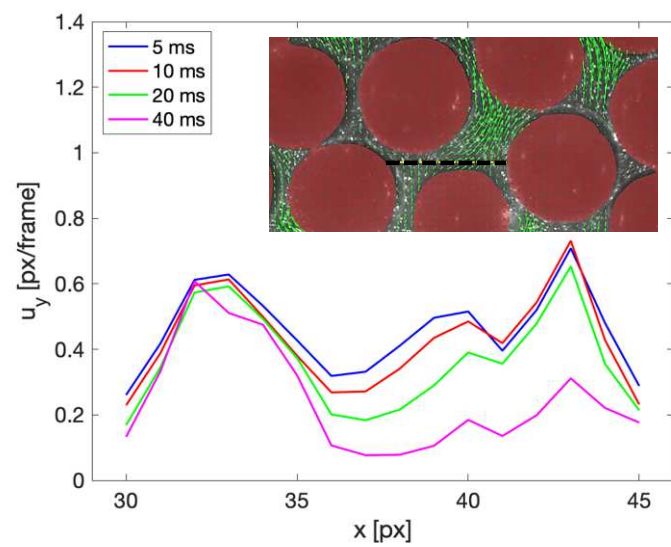
(a)
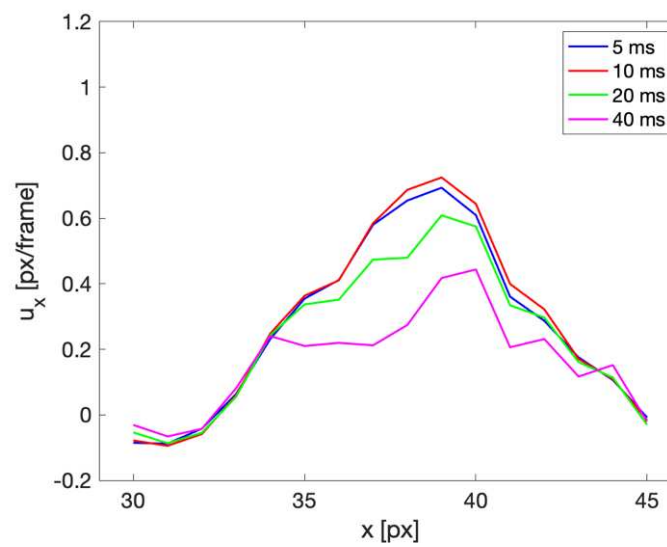
(b)

Figure S2. Distribution of the number of tracers for a subsets of interrogation windows (32 x 32 pixels) for (a) beads and (b) angular particles.
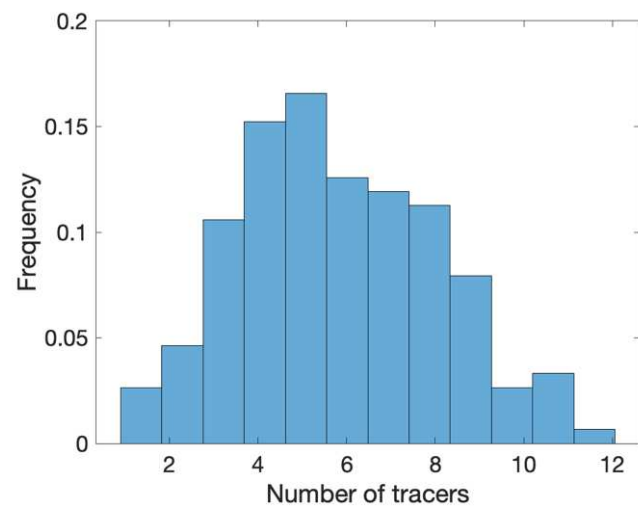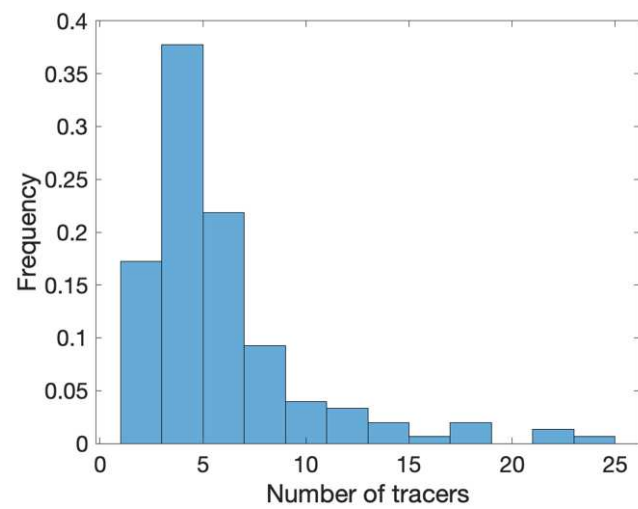
Figure S3. Autocorrelation function for a subsets of interrogation windows (32 x 32 pixels) for (a) beads and (b) angular particles. Histogram of autocorrelation peak width for (c) beads and (d) angular particles.
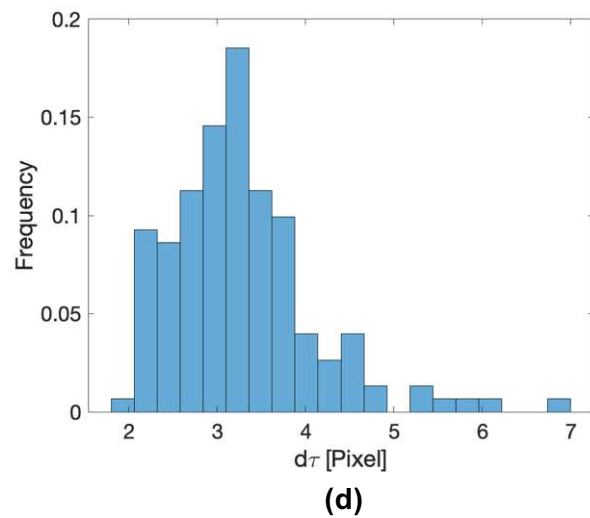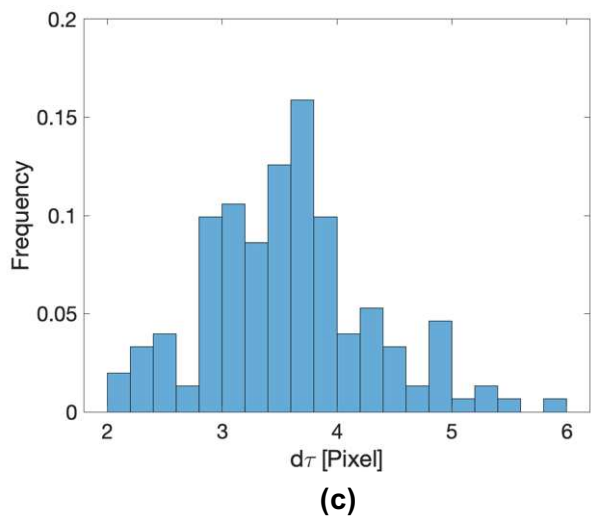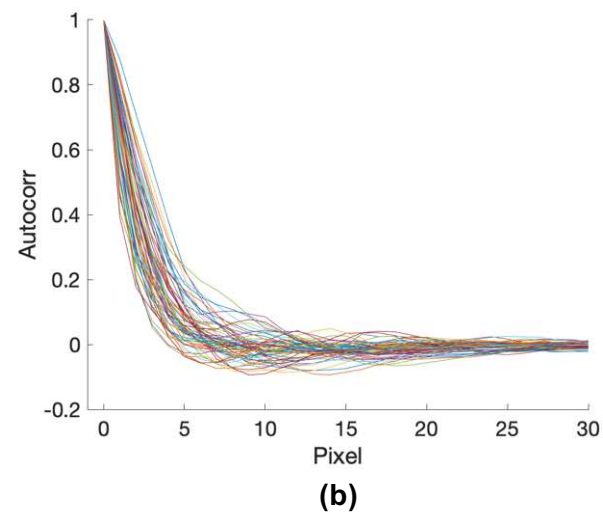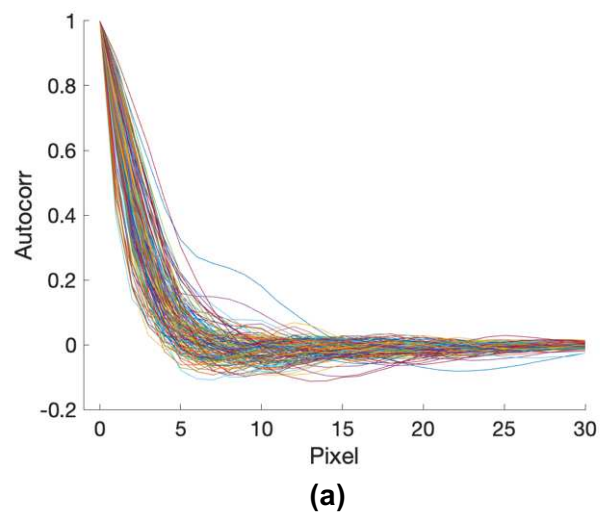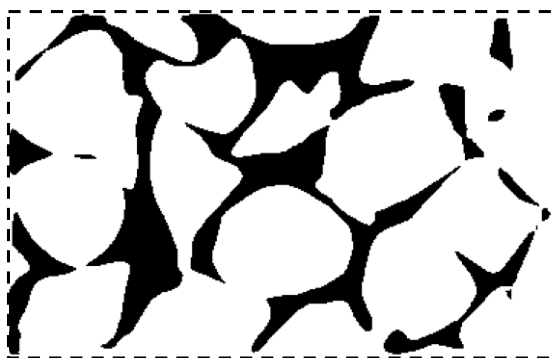
Figure S4. (a) Typical slice of Ang-U processed by U-Net, and the binarization results at different porosity values (b) 0.31, (c) 0.29, and (d) 0.27.
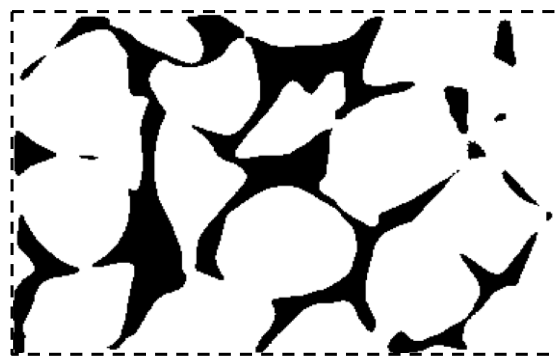

(a)

(b)

(c)

(d)